Frederico Henriques Antão Mendes Tremoço

Bachelor degree in Sciences of Physics Engineering

Heating of Atomic Force Microscopy (AFM) cantilevers operating in liquid media under intense optical illumination

Dissertation submitted in partial fulfillment
of the requirements for the degree of

Master of Science in
Physics Engineering

Adviser: Prof. Dr. Ana Gomes Silva,
Associate Professor,
Universidade Nova de Lisboa

Co-adviser: Dr. Pieter De Beule,
Group Leader,
International Iberian Nanotechnology Laboratory

Examination Committee

Chairperson: Prof. Dr. André João Maurício Leitão do Valle Wemans
Raporteurs: Dr. Luca Costa
Prof. Dr. Ana Gomes Silva

FACULDADE DE CIÊNCIAS E TECNOLOGIA
UNIVERSIDADE NOVA DE LISBOA

January, 2021

Heating of Atomic Force Microscopy (AFM) cantilevers operating in liquid media under intense optical illumination

This document was created using the (pdf)LaTeX processor, based in the "novathesis" template[1], developed at the Dep. Informática of FCT-NOVA [2].
[1] https://github.com/joaomlourenco/novathesis [2] http://www.di.fct.unl.pt

Acknowledgements

I would like to start by thanking those people who expressly or implicitly were essential to this work.
To Dr Pieter de Beule, leader of the Applied Nano-Optics team of the Medical Devices group at International Iberian Nanotechnology Laboratory (INL), I want to thank him for giving me the opportunity to work with him and the team and for all the support he gave me. The guidelines he provided were crucial for the development of this work. I also want to express my gratitude for the personal advice given and shared wisdom.
To Prof Dr Ana Gomes Silva, I want to express my gratitude for being my advisor and for providing me with this wonderful opportunity. I want to acknowledge her for always being available to help and for all the comments and critics provided, which were fundamental in the development of this work and also in my learning path.
To Dr Adelaide Miranda, who kindly helped me and provided me with vital technical information and knowledge, which was crucial for the choices made in this work. I want to also acknowledge her for always being available for help.
To Dr Ana Gomez, who gently provided me with her input on many stages of this project.
To Dr Catarina Moura, member of the Applied Nano-Optics team, who kindly contributed to my integration in the team.
To INL, I want to thank for the opportunity to work on my master thesis in their facilities.
To Beatriz, Jéssica and Tiago, friends that I met in my short stay at Braga, I want to thank for their friendship and for the time we spent together.
I want to acknowledge my colleagues, specially Bruno, Dinis, João Fonseca and João Guerreiro with whom I had the opportunity to work in many academic projects. I also want to highlight their friendship.
Luckily, I have been surrounded by wonderful friends and I am very grateful for their presence and support, not only during my master's, but in my entire life. I hope that we can stay here for a long time and keep on sharing wonderful

moments.
I want highlight Joana for her friendship, love and support. It is a joy and a privilege to share a life with her.
Finally, I want to express to my family my profound gratitude for always being present. Specially to my parents for all the opportunities they have given me and for all their commitment to my education and happiness.
I wish health and all the best for all aforementioned.

Abstract

Atomic Force Microscopy (AFM) has been combined with many optical microscopy techniques to expand the applications and capabilities of both techniques. However, the intense illumination of AFM cantilevers can give rise to a significant temperature increase due to the light power absorption on the gold coating, which is undesirable, especially for live cell imaging.

Computational simulations based on Finite-Difference Time-Domain (FDTD) simulations for electromagnetic wave propagation and absorption combined with a finite element method implementation for thermal simulations were used to study the temperature increase of AFM cantilevers exposed to wide-field and confocal fluorescence illumination.

Our analysis is consistent with a previous study based on a 2D model of a bimetallic strip. It is also observed a strong dependency of the temperature increase on the confocal spot vertical position.

In some simulation's conditions close to experimental set-up configurations we predict with our simulations a temperature increase up to 13 degrees Celcius, a temperature increase which undoubtedly will have an impact on live cell imaging.

We conclude that temperature increases induced by fluorescence excitation light in combined AFM-fluorescence microscopy set-ups can be significant in the sense that they might affect the biological sample under investigation. A proper design of the combined microscopy system is therefore highly recommendable to avoid any potential sample heating artefact.

Resumo

A microscopia de força atómica (AFM) tem sido combinada com diversas técnicas de microscopia óptica de modo a expandir as aplicações e capacidades de ambas. No entanto, a intensa iluminação dos cantilevers de AFM pode originar um aumento significativo da temperatura devido à absorção da luz no revestimento de ouro, o que é indesejável, sobretudo na aquisição de imagens de células vivas.

Foram utilizadas simulações computacionais baseadas em simulações de FDTD (*Finite-Difference Time-Domain*) para propagação e absorção de ondas electromagnéticas combinadas com a implementação de um método de elementos finitos para simulações térmicas, com o objectivo de estudar o aumento da temperatura dos cantilevers de AFM expostos a iluminações de fluorescência *widefield* e confocal.

A nossa análise é consistente com um estudo anterior baseado num modelo 2D de uma tira bi-metálica. Observa-se também uma forte dependência do aumento da temperatura na posição vertical do *spot* confocal.

Em certas condições de simulação próximas das configurações dos set-ups experimentais, prevemos com as nossas simulações um aumento de temperatura até 13 graus Celcius, o que que sem dúvida terá um impacto aquisição de imagens de células vivas.

Concluímos que os aumentos de temperatura induzidos pela luz de excitação em configurações combinadas de AFM com microscopias de fluorescência podem revelar-se significativos no que diz respeito ao facto de poderem afectar a amostra biológica sob investigação. Uma concepção adequada do sistema de microscopia combinada é, portanto, altamente recomendável para evitar qualquer artefacto potencial de aquecimento da amostra.

Contents

List of Figures

List of Tables

Chapter 1

Introduction

1.1 Motivation

The combination of AFM and optical microscopy can further improve the applications and the capabilities of both techniques when it comes to live cell imaging. These improvements can be specially interesting when the two techniques operate simultaneously, since this synchronicity gives the system the capability to follow dynamic biological processes.
There are several problems associated with the simultaneous AFM and optical microscopy data acquisition such as: the cantilever bending induced by the heat generated by the focusing light on the cantilever's gold reflective coating, the perturbation of the AFM performance due to the noise transfer from the optical microscope and the perturbation on the fluorescence acquisition due to the presence of AFM. Furthermore, in some cases the high-powered optical sources, such as the ones using in Stimulated Emission Depletion (STED) microscopy can damage the cantilever's gold coating. Nevertheless, some work has been done to surpass these obstacles [1–3].
The cells activity and dynamics are highly dependent on the environment temperature which makes it important to keep a constant temperature during a live cell image acquisition (37ºC for mammalian cells), however the illumination of the AFM cantilever's gold coating can give rise to an undesired temperature increase in the vicinity of the cantilever, which can lead to wrong observations. This temperature increase can be particularly large when it comes to the interaction of a confocal spot with the cantilever's gold coating.

In order to maintain the certainty that the environment of the performed measurements is as predicted by the theoretical works, regarding live cells dynamics, it is important to have an idea on what temperature increase can be caused by the cantilever illumination.
The combination of optical and thermal simulations has already shown prominent results when it comes to understanding the dynamics of temperature increase in plasmonic nanostructures, when compared with a scanning thermal microscopy setup measurements [4].
The mapping of temperature fields at nanoscale is a great challenge in many nanosciences fields. Computational simulations can be a first approach to better understand the temperature increases in combined AFM/optical microscopy setups.

1.2 State of the art

The Atomic Force Microscope (AFM) was introduced in 1986 by Binning et al.[5] as an extension of the Scanning Tunnelling Microscope (STM), being a new high-resolution technique to probe surfaces of conductors and insulators on an atomic scale, capable of measuring both the interatomic and electromagnetic forces. In this first design, the forces exerted by a surface of a sample on a sharp tip, attached to a ultrasmall mass cantilever beam, were obtained by monitoring the beam deflection with a STM. This system could operate in two modes keeping constant current or height, between the STM tip and the backwards of the beam. In 1987, the first atomic resolution AFM images were presented by Binning et al.[6]. At that time, McClelland et al.[7] presented a new way to measure the cantilever deflection based on optical interference, being more reliable and easier to implement than the tunnelling method achieved with STM. Furthermore, because its lower sensitivity to the roughness of the cantilever, it was pointed as being less affected by the thermal drift reported previously [5, 6].
Nowadays, the cantilever deflection measurement can be achieved by capacitance detection, piezoresistive detection, optical polarization detection, optical interferometry, laser diode feedback and laser beam deflection. The last four are classified as optical techniques and are believed to be more sensitive, reliable and easier to implement [8].
AFM is one of the most versatile instruments in nanotechnology, and its ability to operate in liquid media at ambient temperature makes it a great tool for imaging in biosciences field. For that reason, various modes of operation have been developed in order to expand its possibilities through this field [9].
In order to extend the information collected with AFM, this device has been integrated with diverse optical microscopy techniques [1, 10–21]. More recently, Gómez-Varela et al.[2] achieved the first successful simultaneous operation of Super-Resolution Structured Illumination Microscopy (SIM) and AFM.
One of the greatest limitations in simultaneous operation of AFM and optical fluorescence imaging has to do with an unwelcome cantilever bending due to temperature increase, caused by the interaction between high-powered light sources and the gold reflective coating, typically used in liquid environment to improve AFM laser reflection. On the other hand, this strong illumination can lead to a considerable temperature increase in the surroundings of the cantilever. Miranda et al. [1] used a formulation of Timoshenko's bi-metal thermostats model [22] to associate a Pyrex-Nitride Probe - Triangular cantilever (PNP-TR) a deflection of 9.1 nm to a temperature increase of 0.33ºC, adding that this temperature increase

can affect the samples through heat conduction of the liquid media specially in live cell imaging. Fernandes et al. [3] characterized and quantified radiation pressure, photothermal induced deflection and tip luminescence for three different cantilevers emphasizing the relevance of minimizing this effects in synchronous AFM and fluorescence spectroscopy experiments.
These intense cantilever illumination effects can result in a worse performance and data quality when it comes to simultaneous operation of AFM and fluorescence spectroscopy setups. However, they have been rarely discussed, so work should be done in order to minimize them. There are only two studies made [1, 3], to the best of our knowledge, regarding the temperature increase in combined AFM/optical microscopy set-ups.

1.3 Objectives

This project gives continuity to the International Iberian Nanotechnology Laboratory (INL) Medical Devices group's work of combining optical imaging techniques with AFM operation [1, 2] in order to create new platforms for live cell imaging, a topic that has been studied by some other groups [10–21].
The goal of this work is to use computational simulations to better understand the heating process of the AFM cantilevers when they are exposed to intense illumination schemes in order to evaluate if the temperature increase forced by the light absorption on the cantilever's gold coating is suitable for live cell imaging, specially regarding live cell dynamics. [23].

1.4 Document overview

This document addresses the work developed during the master thesis program and it is divided in five main chapters, the first of which is the introduction chapter.
Chapter 2 brings together all the relevant theoretical aspects behind the computational simulations. It is divided in two main parts where the first one is a more general theoretical section and the second one is dedicated specifically to the two solvers used for the simulations.
Chapter 3 shows and justifies the procedures and choices made in the models development. It starts by presenting the cantilevers that where chosen to be modeled. Then the two different simulations (optical and thermal) are presented in separated sections. In both cases the common aspects to all the simulations are presented firstly and then the specification arises.
Chapter 4 presents and discusses the results. It is divided in four sections: the first one presents the temperature increase profiles for both simulated cantilever types obtained considering a widefield illumination scheme, the second one contains the same kind of results considering a confocal illumination schemes, the third one is an overview of the maximum temperature increases reached in all the simulated situations and the final one is where the results are discussed.
Chapter 5 states the conclusions of this work and mentions some work that could be interesting to be done in the future regarding this topic.

Chapter 2

Theoretical concepts

This chapter presents the fundamental theoretical concepts that sustain this work. It starts by a formal presentation and description of the electromagnetic waves propagation in matter which starts by presenting the Maxwell's equations in matter and follows by describing the concepts associated to electromagnetic waves propagation in matter.
It follows a mathematical description of the FDTD process which contains a formal description of the original FDTD algorithm and goes further to describe important concepts related to Lumerical's FDT solver.
Finally a description of the Lumerical's HEAT solver is presented.

2.1 Electromagnetic waves in matter

There are several ways to write the Maxwell Equations, in this case it is required to understand electromagnetic phenomena in conducting and insulating media. This sections aims to cover the necessary theory for the understanding of the phenomena. This treatment was adapted from reference [24], where more details can be found.

2.1.1 Maxwell's Equations in matter

Maxwell's Equations are a well know description of the electric and magnetic fields and their mutual relation. When it comes to describe this phenomena in matter they can be written in differential form as:

$$\overrightarrow{\nabla} \cdot \overrightarrow{D} = \rho_f, \tag{2.1}$$

$$\overrightarrow{\nabla} \times \overrightarrow{E} = -\frac{\partial \overrightarrow{B}}{\partial t}, \tag{2.2}$$

$$\overrightarrow{\nabla} \cdot \overrightarrow{B} = 0, \tag{2.3}$$

$$\overrightarrow{\nabla} \times \overrightarrow{H} = \overrightarrow{j_f} + \frac{\partial \overrightarrow{D}}{\partial t}, \tag{2.4}$$

Where ρ_f and $\overrightarrow{j_f}$ are, respectively, the free charge density and free current. The "free" stands for the fact that they only depend on external sources, *i.e* they do not take into account the bound charges, bound currents and the polarization currents, these are included in $\overrightarrow{H}$ and $\overrightarrow{D}$, the electric displacement and magnetic fields respectively. The $\overrightarrow{E}$ and $\overrightarrow{B}$ fields are, respectively, the electric and magnetic induction fields and, considering a linear and isotropic medium, they can be related to $\overrightarrow{D}$ and $\overrightarrow{H}$ fields as follows:

$$\overrightarrow{D} = \epsilon \overrightarrow{E} \tag{2.5}$$

and

$$\overrightarrow{H} = \frac{1}{\mu} \overrightarrow{B}. \tag{2.6}$$

The ϵ and μ are the electric permitivity and magnetic permeability of the medium, respectively. This formulation of the Maxwell's Equations is useful in a way that allows the fields to be written in terms of free charges and currents.
Another important result that can be derived from the Maxwell's Equations is the continuity equation, which states the equality between the decrease of charge within a differential volume and the flux of current outwards that volume:

$$\frac{\partial \rho_f}{\partial t} = -\overrightarrow{\nabla} \cdot \overrightarrow{J_f} \tag{2.7}$$

In order to have the complete mathematical set to describe electromagnetic waves we should introduce the Ohm's Law (eq.2.8), which establishes the proportionality relationship between the electric field and the free current density,

$$\overrightarrow{J_f} = \sigma \overrightarrow{E}. \tag{2.8}$$

σ denotes the electrical conductivity (inverse of resistivity) which measures the ability of a material to conduct electrical currents, this constant vanishes for perfect insulators and takes an infinite value for perfect conductors.

2.1.2 Electromagnetic waves in matter

Applying the curl operations to equations 2.2 and 2.4, taking into account the remaining Maxwell equations, and considering eq.2.7 and eq.2.8 :

$$\nabla^2 \overrightarrow{E} = \epsilon\mu \frac{\partial^2 \overrightarrow{E}}{\partial t^2} + \mu\sigma \frac{\partial \overrightarrow{E}}{\partial t}, \tag{2.9}$$

and

$$\nabla^2 \overrightarrow{B} = \epsilon\mu \frac{\partial^2 \overrightarrow{B}}{\partial t^2} + \mu\sigma \frac{\partial \overrightarrow{B}}{\partial t}. \tag{2.10}$$

These equations regard light as an electromagnetic wave in which electric and magnetic fields propagate perpendicular to each other and to the direction of propagation. In this context one can evaluate the monochromatic plane-wave solutions for $\overrightarrow{E}$ and $\overrightarrow{B}$ fields travelling in z-direction as follows:

$$E(z,t) = E_0 e^{-Im(k)z} e^{i[Re(k)z - \omega t]} \quad E, E_0 \in \mathbb{C}, \tag{2.11}$$

and,

$$B(z,t) = B_0 e^{-Im(k)z} e^{i[Re(k)z - \omega t]} \quad B, B_0 \in \mathbb{C}. \tag{2.12}$$

Where ω is the angular frequency of the wave and k is the complex wave number with the following real and imaginary parts:

$$Re(k) = \omega \sqrt{\frac{\epsilon\mu}{2}} \left[\sqrt{1 + \left(\frac{\sigma}{\epsilon\mu} \right)^2} + 1 \right]^{\frac{1}{2}} \tag{2.13}$$

and,

$$Im(k) = \omega \sqrt{\frac{\epsilon\mu}{2}} \left[\sqrt{1 + \left(\frac{\sigma}{\epsilon\mu} \right)^2} - 1 \right]^{\frac{1}{2}} \tag{2.14}$$

Equations 2.11 and 2.12 describe a propagating wave with an amplitude modulation governed by the imaginary part of the wave vector.
For vacuum and insulating media one can consider the free charges and currents to be zero which implies the eliminations of the second terms of eq.2.9 and eq.2.10 which is consistent with the fact that for low conductivity the imaginary part of the wave number vanishes.
For conductors the previous assumption is not valid so in this case the wave attenuation plays a big role.

2.2 Computational simulations

Lumerical is a high-performance photonic simulation software [23] composed of several solvers and tools.
In this section, the Finite Difference Time Domain (FDTD) and HEAT solvers, used in this project, will be presented. In both solvers one needs to define a geometry through a computer aided design (CAD) interface included on the software (it is also possible to import CAD files from other CAD softwares). Then it is required to assign materials to the simulation objects, define boundary conditions and place monitors which will be the measurement tools of the desired quantity. This whole process can be executed manually or with scripting in a specific language (Lumerical scripting language).
This section starts describing the FDTD solver and then goes to a description of the HEAT solver.
For further knowledge on this one should consider the reference manual of each solver [25] and [26].

2.2.1 Finite Difference Time Domain (FDTD) method

The Lumerical's FDTD method [25] is a Finite Difference Method (FDM) for solving Maxwell's Curl Equations (eqs.2.2 and 2.4) in complex geometries of non-magnetic materials ($\mu \approx \mu_0$, which implies $\mu_r \approx 1$).
The FDTD method was proposed by Yee [27] in 1966. In this approach the geometry of the simulation is divided into a mesh composed of individual cells (called unitary cells or Yee cells). Each component of both fields is calculated in a different region of the Yee cells. The electric field components are calculated in the middle of the edges and the magnetic field components in the center of the faces.

In a cartesian coordinate system, like the one in figure 2.1, we can write equations 2.2 and 2.4 for each field component as follows:

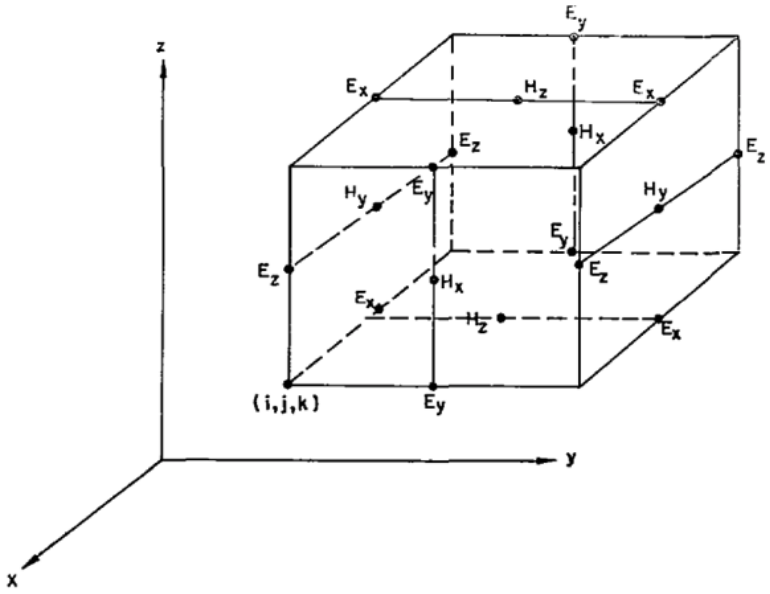

Figure 2.1: Representation of the unitary cell and the location of each calculated component of both fields. [27]

$$-\frac{\partial B_x}{\partial t} = \frac{\partial E_z}{\partial y} - \frac{\partial E_y}{\partial z}, \tag{2.15}$$

$$-\frac{\partial B_y}{\partial t} = \frac{\partial E_x}{\partial z} - \frac{\partial E_z}{\partial x}, \tag{2.16}$$

$$-\frac{\partial B_z}{\partial t} = \frac{\partial E_y}{\partial x} - \frac{\partial E_x}{\partial y}, \tag{2.17}$$

$$\frac{\partial D_x}{\partial t} = \frac{\partial H_z}{\partial y} - \frac{\partial H_y}{\partial z} - j_{f_x}, \tag{2.18}$$

$$\frac{\partial D_y}{\partial t} = \frac{\partial H_x}{\partial z} - \frac{\partial H_z}{\partial x} - j_{f_y}, \tag{2.19}$$

$$\frac{\partial D_z}{\partial t} = \frac{\partial H_y}{\partial x} - \frac{\partial H_x}{\partial y} - j_{f_z}. \tag{2.20}$$

$$\tag{2.21}$$

The FDTD method then consists in solving these equations for each cell by calculating numerically the derivatives replacing them by finite differences [1].

[1] For example for equations 2.15 and 2.18, according to figure 2.1 we have [27]:
$\frac{B_x^{n+1/2}(i,j+1/2,k+1/2)-B_x^{n-1/2}(i,j+1/2,k+1/2)}{\Delta t} = \frac{E_y^n(i,j+1/2,k+1)-E_y^n(i,j+1/2,k)}{\Delta z} - \frac{E_z^n(i,j+1,k+1/2)-E_z^n(i,j,k+1/2)}{\Delta y}$ and
$\frac{D_x^n(i+1/2,j,k)-D_x^{n-1}(i+1/2,j,k)}{\Delta t} = \frac{H_z^{n-1/2}(i+1/2,j+1/2,k)-H_z^{n-1/2}(i+1/2,j-1/2,k)}{\Delta y} -$
$-\frac{H_y^{n-1/2}(i+1/2,j,k+1/2)-H_y^{n-1/2}(i+1/2,j,k-1/2)}{\Delta z} + j_{f_x}^{n-1/2}(i+1/2,j,k).$
Where any function of space and time is represented as follows : $F(i\Delta x, j\Delta y, k\Delta z, n\Delta t) = F^n(i,k,k)$.

The mesh step-size of the simulation region is automatically generated by default and this algorithm is set to keep a constant of mesh points per wavelength.
For 2D simulations, the system is considered to be infinite in z-direction, which means that the material's properties (eq.2.22) and the fields (eq.2.23) are not dependent on the z-coordinate. These considerations are condensed below:

$$\epsilon(\omega, x, y, z) = \epsilon(\omega, x, y), \tag{2.22}$$

and

$$\frac{\partial \overrightarrow{E}}{\partial z} = \frac{\partial \overrightarrow{H}}{\partial z} = 0. \tag{2.23}$$

As expected 2D simulations are used, when the system's symmetry allows, to reduce the computational memory and time required.

2.2.1.1 Optical power absorption

To model an AFM cantilever under intense illumination it is used a plane-wave light source or a gaussian source which focus perpendicularly on cantilever's bottom surface which is exposed to incoming light. Then the power absorbed by the cantilever is calculated.
The absorbed power per unit volume P_{abs} can be obtained by three different methods: simple method, advanced method and divergence of Poynting vector method. Once calculated the power absorbed per unit volume, the total absorbed power can be obtained integrating over the entire volume.
The absorption per unit volume can be derived from the Poynting vector ($\overrightarrow{S}$) by calculating its divergence [25]:

$$P_{abs} = -\frac{1}{2} real(\overrightarrow{\nabla} \cdot \overrightarrow{S}), \tag{2.24}$$

this is the equation used by divergence of Poynting vector method. This is not the best equation to use, due to high sensitivity of divergence calculations to numerical approaches, as it is shown in reference [28]. Considering exponential representation of electromagnetic waves we can verify that last equation is equivalent to:

$$P_{abs} = -\frac{1}{2} real(i\omega \overrightarrow{E} \cdot \overrightarrow{D}), \tag{2.25}$$

That finally can be written as [25]:

$$P_{abs} = -\frac{1}{2} \omega \left| \overrightarrow{E} \right|^2 imag(\epsilon), \tag{2.26}$$

This equation is used by the simple method to calculate P_{abs}, it should be noted that these quantities can be easily obtained with Lumerical. For a detailed discussion of these equations one should consider section 6.8 of the reference [29].
In the FDTD method each field component is calculated in a different location of the Yee cell and, to simplify, FDTD interpolates each field component back to the cell origin to perform a simpler and faster computation. The advanced mode doesn't use this interpolation so it can yield more accurately results, although it implies higher computational costs.

2.2.1.2 Lumerical's frequency domain continuous wave normalization

Instead of performing a simulation for each frequency (with a different light wavelength) when broadband results are needed, Lumerical, by default (this feature can be disabled) performs a unique simulation using a signal pulse **s(t)**. The spectrum of the source pulse is given by its Fourier transform:

$$s(t) \xrightarrow{\mathscr{F}} s(\omega), \quad s(\omega) = \int exp(i\omega t)s(t)dt.$$

The field monitors (simulation objects) collect the electric field in each cell as a time function $\overrightarrow{E}(t)$ and evaluate the system response $\overrightarrow{E}(\omega)$ which are related by a Fourier transform, as well:

$$\overrightarrow{E}(t) \xrightarrow{\mathscr{F}} \overrightarrow{E}(\omega), \quad \overrightarrow{E}(\omega) = \int exp(i\omega t)\overrightarrow{E}(t)dt.$$

The frequency domain continuous wave normalization [30] consists in returning $\overrightarrow{E}(\omega)$ normalized to the source spectrum (also known as the impulse response of the system), instead of returning just $\overrightarrow{E}(\omega)$. Therefore we have:

$$\overrightarrow{E}_{norm}(\omega) = \frac{\overrightarrow{E}(\omega)}{s(\omega)}, \tag{2.27}$$

which is independent of the the source pulse.

2.2.1.3 Lumerical's auto non-uniform mesh

In the original Yee-cell FDTD algorithm, the simulation region is discretized into a uniform Cartesian mesh.
The Lumerical's auto non-uniform mesh algorithm generates a rectangular mesh in which the cells have different sizes according to the material within them [31]. The non-uniform meshes allows the FDTD to have more accurate solutions while requiring less memory and computational time as well, which happens because in

the regions where there is no need for such a thinner mesh the algorithm generates a coarse one.
An important measure of accuracy in the FDTD methods is the number of cells per wavelength (N):

$$N = \frac{\lambda_0}{nD}, \tag{2.28}$$

where λ_0 is the wavelength in free space, n is the refractive index[2] and D is the mesh cell size (in the direction of propagation). A small number of points per wavelength results in a poor space sampling which is the cause of numerical dispersion (difference between the speed of light propagation in the material in the FDTD simulation and in reality).
Using the auto non-uniform mesh algorithm the mesh is created based on the materials used, keeping the number off cells per wavelength constant in the whole simulation region, leading to a smaller mesh in materials with a higher refractive index[3] (in cases where index of refraction is a complex number, both real and imaginary parts are considered, to maintain enough points per wavelength and per decay length [4]).
Since this is an automatic algorithm the user can only set the mesh accuracy from integer values between 1 and 8 which have a correspondence in number of cells per wavelength stated on table 2.1.

Table 2.1: Correspondence between mesh accuracy and number of cells per wavelength on the auto non-uniform mesh algorithm.

Mesh precision	Number of cells per wavelength (N)
1	6
2	10
3	14
4	18
5	22
6	26
7	30
8	34

It is possible to further constraint the mesh step sizes in some areas of the simulation region using the "mesh override" object, which may be useful for better resolve interfaces in some structures, nevertheless it can increase significantly the

[2] $n \approx \sqrt{\frac{\epsilon}{\epsilon_0}}$

[3] One should consider the refraction phenomena where the wavelength in the material is related with the wavelength on vacuum by: $\lambda = \frac{\lambda_0}{n}$

[4] Due to optical absorption

simulation time and memory requirements, therefore the user should be prudent using this.

Table 2.2: Relationship between simulation memory and time requirements, for 2D and 3D simulations, and the mesh step size dx, the volume V or area A and the wavelength λ [25]

	3D	2D
Memory Requirements	$\propto V(\lambda/dx)^3$	$\propto A(\lambda/dx)^2$
Time	$\propto V(\lambda/dx)^4$	$\propto A(\lambda/dx)^3$

Furthermore the interfaces between different materials can be better resolved using Lumerical's conformal mesh technology (CMT), which is a method that calculates exactly the Maxwell's integral equations near interfaces between two different materials, taking into account the material's fit of the permitivity (*cf.* further in section 3.2.1). This provides a greater accuracy for a specific mesh size without requiring significantly more simulation time and memory.

2.2.2 HEAT solver

The Lumerical's HEAT solver [26] is a Finite Element Method (FEM) that solves the heat transport equation on a finite-element triangular mesh in two or three dimensions:

$$\rho c_p \frac{\partial T}{\partial t} - \overrightarrow{\nabla} \cdot (k \overrightarrow{\nabla} T) = Q, \tag{2.29}$$

giving a solution for T (temperature in Kelvin). Where ρ stands for mass density (kg/m^3), c_p for specific heat (J/kg.K), k for thermal conductivity (W/m.K) and Q for the applied heat energy transfer rate (W/m^3).
For constant temperature (steady-state) solutions it arises:

$$- \overrightarrow{\nabla} \cdot (k \overrightarrow{\nabla} T) = Q, \tag{2.30}$$

which is what we are looking for.In comparison with FDTD solvers, the HEAT solver has quite a different way of compute the problems. In the first one, as we already present, differential equations are solved through finite differences in a discrete spacial and temporal mesh, the initial conditions are set by the source (which defines the initial energy pulse) and the boundary conditions defined by the user. In case of the HEAT solver, the user needs to specify through boundary conditions a temperature at a given point in space and the heat sources. Then the software seeks for a solution (through numerical methods) that comprises all

the constraints, which is more like solving an optimization problem. Sometimes the solver does not converge to a solution in a specific simulation design hence tests are needed to be performed with different conditions and in some cases it is required to enlarge the maximum number of iterations performed by the solver in order to have a solution, which requires more time and computational resources.

Chapter 3

Methodology

Two types of computational simulations were performed: optical and thermal. The optical simulations are used to model the light propagation and the power absorption on the cantilever's gold coating. The thermal simulations are then used to associate the absorbed light power to an heat source in order to model the temperature increase.
This chapter contains the information regarding the simulations performed.
In the first section there is a description of the studied cantilevers.
In the second section the optical simulations are presented. It starts by presenting the common aspects to all the optical simulations and then it introduces the two types of optical simulations performed.
In the third section the methodologies for thermal simulations are stated. It starts, like the previous section, with general followed by a specific presentation of each simulation type.

3.1 Studied Cantilevers

This section contains relevant information about the simulated cantilevers. These cantilevers are divided in two families which are the PNP-TR and qp-BioAc cantilevers and these are two widely used cantilever types in the biosciences field. Firstly the PNP-TR cantilevers are presented followed by the qp-BioAc cantilevers.

3.1.1 Pyrex-Nitride Probe - Triangular (PNP-TR) cantilevers

Pyrex-Nitride probes by Nanoworld® are pyrex-glass support chips containing 4 triangular cantilevers of two different sizes (two cantilevers of each size). These cantilevers are made of silicon nitride and have a gold coating to enhance the reflectivity of the detection laser in liquid media.
The nominal values of the PNP-TR cantilever type's data can be found on table 3.1.
The type 1 PNP-TR cantilever was used by Miranda et al.[1] to make the first study on the temperature increase caused by illumination light in a combined AFM/DSD (differential spinning disk) microscopy set-up and it is the one studied in the work presented herein, anyway the obtained results are expected to be analogous for the type 2 PNP-TR cantilevers.

Table 3.1: PNP-TR cantilever types data (nominal values). Data taken from reference [32].

	Length (μm)	Thickness (nm)	Mean width (μm)	Force constant (N/m)	Resonance frequency (kHz)
Type1	100	500	13.5	0.32	67
Type2	200	500	28	0.08	17

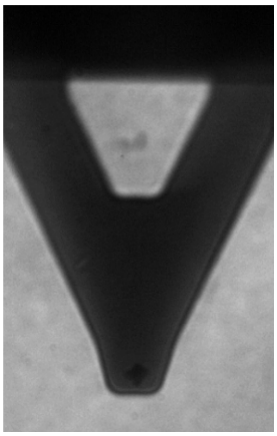

Figure 3.1: PNP-TR type1 cantilever (adapted from [1]).

3.1.2 qp-BioAc cantilevers

The Nanosensors® qp-BioAc are soft rectangular cantilevers designed for biological and life sciences purposes. These cantilevers are made of silica (SiO_2) and have got a partial 60 nm gold coating, that covers only the free end of the cantilever (in order to avoid undesirable bending), to enhance the reflectivity of the positioning light in liquid media.
The probe's support chip contains three different cantilevers (CB1, CB2 and CB3)

whose characteristics are listed in table 3.2. These three cantilever types were simulated in the present work.
The support chip containing the three different cantilevers can be seen in figure 3.2.

Table 3.2: qp-BioAc cantilevers data (nominal values). Data taken from reference [33].

	Length (μm)	Thickness (nm)	Mean width (μm)	Force constant (N/m)	Resonance Frequency (kHz)
CB1	40	400	20	0.3	90
CB2	60	400	25	0.1	50
CB3	80	400	30	0.06	30

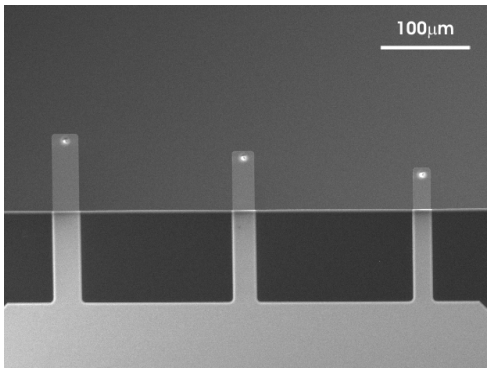

Figure 3.2: qp-BioAc support chip containing the three cantilevers (CB1, CB2 and CB3)[33].

3.2 Optical simulations

Two kinds of optical simulations were performed: the wide-field illumination simulations which aim to model optical set-ups where the light covers the entire surface of the cantilever and the confocal illumination simulations which aim to model the interaction between a confocal spot placed in different vertical positions and the gold coating of each cantilever.
Since they are very small compared to the cantilevers, the tips were not included in the designed geometries, however they would not reproduce significant differences in the results.
FDTD simulations constitute a set of iterations whereby an initial guess is taken and through a series of numerical iterations, a convergence to a solution of the posed problem is obtained. It is important to evaluate this convergence in order to mitigate the associated numerical errors.
This section begins with the description of the common aspects of both simulation's types (including materials, monitors and convergence testing process)

followed by a specific description of the details of each simulation type, where the widefield illumination and confocal illumination optical simulations are described, respectively.

3.2.1 Materials

The light waves propagation and absorption in materials are governed by real and imaginary parts of refractive index[1] which can take different values for different frequencies (in case of dispersive materials). Lumerical's default materials database includes experimental data points for real and imaginary parts of relative electrical permitivity (ϵ_r) at different frequencies for many materials. Since these data points are discrete and simulations are performed for a continuous broadband, the software contains an automatically generated fit whose parameters can be adjusted with respect to the broadband, thus it can be better adjusted to the experimental data. There are more than one available choices for the same material in the default database, therefore they were chosen accordingly to the best fits for the working broadband. Since in every kind of FDTD simulations the results are highly dependent on the materials, it is important to allocate some time to find the best fits and material. This section comprises all the information, about the materials, one needs to replicate the optical simulations performed.

- **Gold**: Au (Gold) - CRC [2];
- **Silicon nitride**: Si_3N_4 (Silicon Nitride) - Phillip [3];
- **Water**: H_2O (Water) - Palik [4];
- **Silica**: SiO_2(Glass) - Palik.

Lumerical's default options generate in general quite good fits. However to improve the fit's quality, some properties, listed below, have to change:

- **Fit tolerance**: Sets the target root mean square error (RMSE)[5] of the fit. The fitting algorithm returns the model which has the smallest number of coefficients and has an RMSE below the tolerance. This tolerance was set to zero in every fit which allows the software to select the best fit possible,

[1] $n^2 \approx \epsilon_r$, considering $\mu_r \approx 1$.
[2] CRC Handbook of Chemistry & Physics
[3] H. R. Philipp. Optical properties of silicon nitride, J. Electrochim. Soc. 120, 295-300 (1973)
[4] Handbook of Optical Constants of Solids I - III by E. Palik
[5] $RMSE = \sqrt{\frac{\sum_{i=1}^{n}(\hat{y}_i - y_i)^2}{n}}$, where $\hat{y}_i$ are the predicted fit values, y_i are the real data values and n is the number of data points.

without being constrained by the number of coefficient used. By default this is set to 0.01 but this value is highly recommended (by Lumerical team) to be changed to zero, so the best can be found, respecting the other constraints;

- **Max coefficients**: Sets the maximum number of allowed coefficients, one should consider that the introduction of more coefficients in the fits have computational costs of memory and time. Furthermore, although raising coefficients usually leads to a decreasing in the RMSE, it is well known that lower RMSE doesn't always mean a better fit, since RMSE is an average measurement. This is set to 6 by default, but, by setting fit tolerance to 0, one should check if the number of coefficients used is below 6, otherwise it could mean that an increase in the max number of coefficients may lead to a better fit;

- **Imaginary weight**: This sets how much consideration (weight) is given to the imaginary part (an imaginary weight of 2 gives 2 times more weight to the imaginary part and an imaginary weight of 0.5 gives 2 times more weight to the real part), comparing to the real part, which can be useful when one of the parts is much smaller than the other. When imaginary weight is different than 1, the algorithm will try to achieve a weighted RMSE[6] lower than the specified tolerance (if this is set to zero the algorithm chooses the smaller);

- **Fit range**: This is set to be the source bandwidth by default, which was kept in our simulations;

- **Make fit passive and improve stability**: These two options are toggled by default. The first one aims to prevent the fit from having gain at any frequency. The second one aims to reduce numerical instabilities limiting the number of coefficients. These two options were preserved in their original state.

The figures 3.3, 3.4, 3.5 and 3.6 show the fits of the real an imaginary parts of relative electrical permitivity for each material.
In case of gold's fit the imaginary weight was set to 2, otherwise the fit would produce big errors in some points of the imaginary part. This fit has got 8 coefficients and generates an RMSE of 0.036 (approximately) and an weighted RMSE of 0.026 (approximately). The left-side plot of figure 3.3 makes clear that the

[6]This consists in, instead of giving the same weight 1/n to each term of the summation in RMSE, weighting each value in the summation according to the chosen imaginary weight

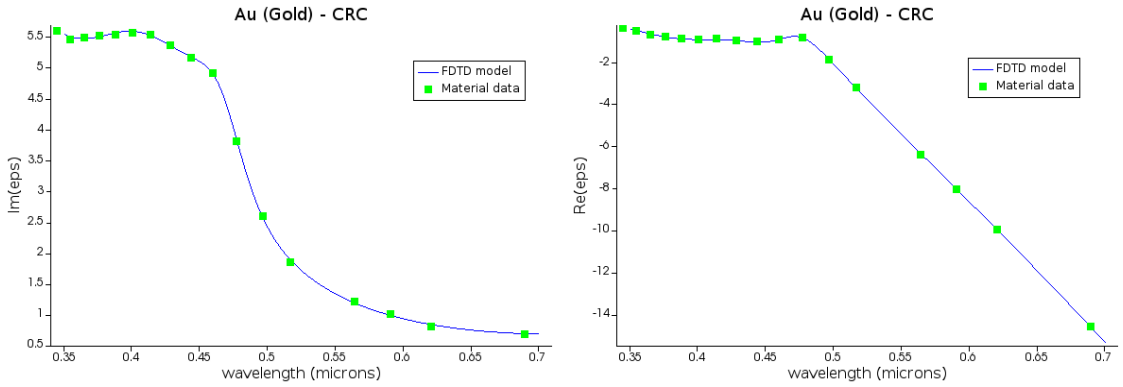

Figure 3.3: Experimental data and fitting for the imaginary and real parts of gold's electrical permitivity. The imaginary part is represented on the left-side plot and the real part on the right-side plot.

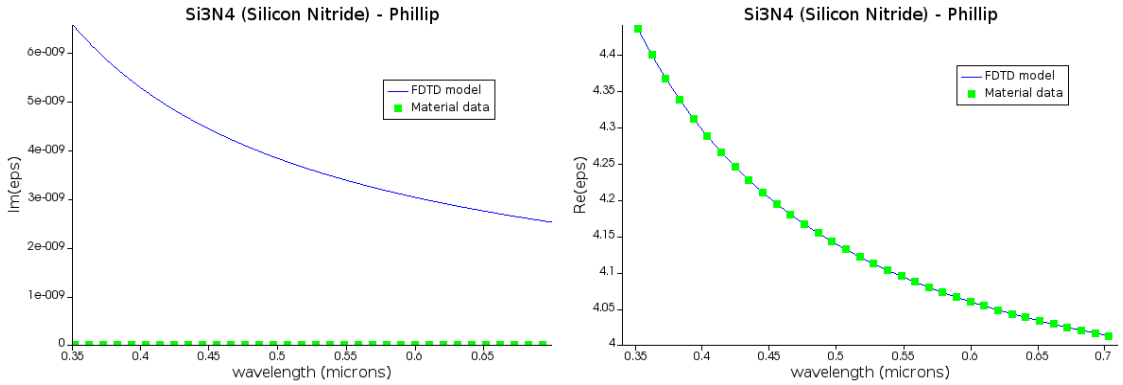

Figure 3.4: Experimental data and fitting for the imaginary and real parts of silicon nitride's electrical permitivity. The imaginary part is represented on the left-side plot and the real part on the right-side plot.

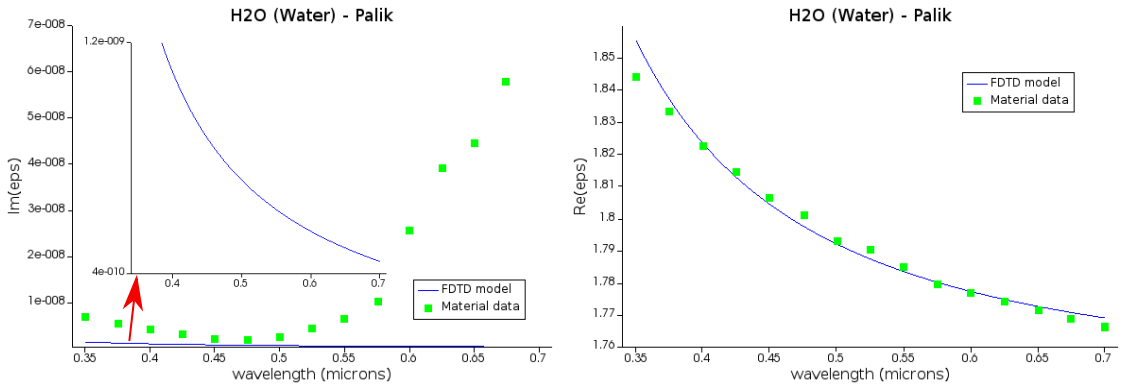

Figure 3.5: Experimental data and fitting for the imaginary and real parts of water's electrical permitivity. The imaginary part is represented on the left-side plot and the real part on the right-side plot. For this fit the imaginary weight was set to 1.

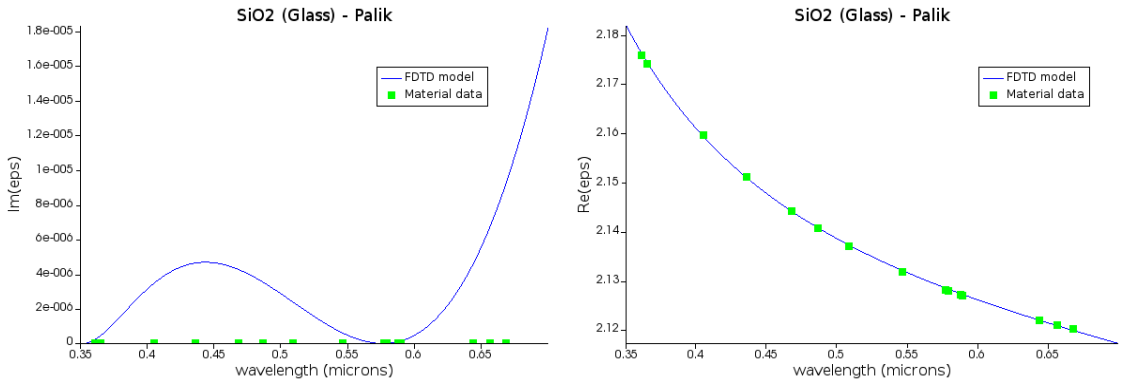

Figure 3.6: Experimental data and fitting for the imaginary and real parts of silica electrical permitivity. The imaginary part is represented on the left-side plot and the real part on the right-side plot.

gold's optical power absorption, as expected and according to equation 2.26, is significant, specially when compared with the other materials.

In case of silicon nitride's fit the imaginary weight was set to 1. This fit has got 6 coefficients and generates an RMSE of 2.23e-9. Despite experimental data suggests that the imaginary part of silicon nitride's permitivity is 0 for the whole broadband, it was impossible to find a better fit, nevertheless the amount of power absorbed because of this difference can be obviously neglected due to the fact that the fitted values are very orders of magnitude inferior to the unity.

In case of water's fit it has got 6 coefficients and generates an RMSE of 0.002. Looking to the imaginary part of the water's electrical permitivity one can easily see that there is some absorption in water not being considered (the fit for its imaginary part of relative electrical permitivity has got lower values than the experimental data) in simulations which in one hand enable us to perform the simulations with the source closer to the cantilever in order to reduce the required computational resources, but in the other hand, can lead to a slightly bigger absorption on gold coating than it happens in reality. Nonetheless one should bear in mind that, even considering the experimental data values for ϵ_r, the absorption in water can be neglected for this wavelength range since they have a very low order of magnitude compared with absorptive materials such as gold.

Finally in case of silica's fit the imaginary weight was set to 10. This fit got 5 coefficients and generates an RMSE of 2.51e-4 and a weighted RMSE of 2.54e-5. Likewise the case of silicon nitride, the experimental data for the imaginary part of electrical permitivity for the silica is zero in the whole broadband but the fit doesn't exactly reproduce this, allowing a low absorption on the silica which can be neglected as well.

3.2.2 Monitors

The monitors are simulation objects capable of collect desired results or quantities on a specified area or volume of the simulation region. These quantities are acquired in discrete points.
In our simulations the gold coating of the cantilevers was surrounded by an advanced power absorbed analysis group, which is a container of frequency-domain field and power and refractive index monitors (capable of collecting the field and the refractive index in each cell for each frequency). This container calculates the absorbed power per unit volume (equation 2.26) for each desired frequency point and then performs an integration over the entire volume or area (*cf.* section 2.2 of theoretical concepts chapter) in order to calculate the total power absorbed.

3.2.3 Convergence testing

Although there are several parameters that affects convergence in most FDTD simulations, in our case, it was noted that the only parameter playing a big role in results convergence was the mesh size, which is typically a crucial parameter since we are approximating infinitesimals with finite differences.
The convergence testing procedure evaluates the impact in the results caused by a change in a parameter (directly related with the simulation's accuracy), comparing to the last execution. For a solid simulation it is expected that the increasing of the accuracy above a certain point doesn't change the results, considerably.
The level of convergence can be quantified using the expression below [34]:

$$\Delta\sigma(i) = \sqrt{\frac{\int(\sigma_i - \sigma_{i-1})^2 d\lambda}{\int(\sigma_i)^2 d\lambda}}, \tag{3.1}$$

Where σ_i and σ_{i-1} stand for the result (fraction of absorbed power in our case) in each wavelength point of the source spectrum in two consecutive realizations of the simulation where the i parameter (mesh accuracy, in our case, since we have used conformal mesh technology, *cf.* section 2.2 of the theoretical concepts chapter) is changed.
In fact since we evaluate the results in discrete points, the integrals in last equation can be regarded as sums.
Having a convergence means that the value of $\Delta\sigma(i)$ tends to zero as the simulation accuracy and computational and time costs increase, through the rising of the i parameter.
Furthermore a decrease in $\Delta\sigma(i)$ should be observed as i parameter is increased, otherwise, if at any moment it is observed a big increase in this value it means

that at that values of the i parameter there are other sources of error playing a bigger role in the simulation accuracy.

3.2.4 Wide-field illumination optical simulations

In the wide-field illumination set-ups the light illuminates the whole sample and the resultant fluorescence is detected. Optical sectioning [7] can be achieved using a pinhole or a differential spinning disk (DSD) as presented by Miranda et al. [1] where optical sectioning is achieved using an incoherent light source and a DSD. When combined with AFM microscope this illumination covers the whole cantilever. In our simulations we model this kind of set-ups using a plane wave that covers all the simulation region illuminating the modeled cantilever.
Because of hardware limitations we evaluated the possibility of model these set-ups using a 2D simulation which is further presented.
In this section one can find described the source and the boundary conditions for this kind of simulations. The differences between the 2D and 3D approaches are discussed related to accuracy. Furthermore the geometries and convergence testing for each cantilever type are presented.

3.2.4.1 Source

In order to obtain the fraction of incident power absorbed on the gold coatings for a useful band of wavelengths, a plane-wave source with a broadband from 350 to 700 nm (which covers the relevant broadband for live cell microscopy) is used. A plot of the source spectrum and pulse can be found in figure 3.7. It is important to note that there is no need to specify the power of the source due to the continuous wave normalization (*cf.* section 2.2 of theoretical concepts chapter). As we saw previously, the light absorption in water is negligible. In order not to extend the simulation region, which has a huge computational cost, the plane wave source is placed right below the cantilevers.

3.2.4.2 Boundary conditions

To allow the light to propagate uniformly in y-direction, the boundaries were defined to be periodic in x-direction and Perfect Matched Layer (PML) in y-direction (the software considers 8 PML layers by default, it was confirmed that the increase of this amount in our case doesn't make any change in the final result) which are

[7] Process to construct a 3D sample image

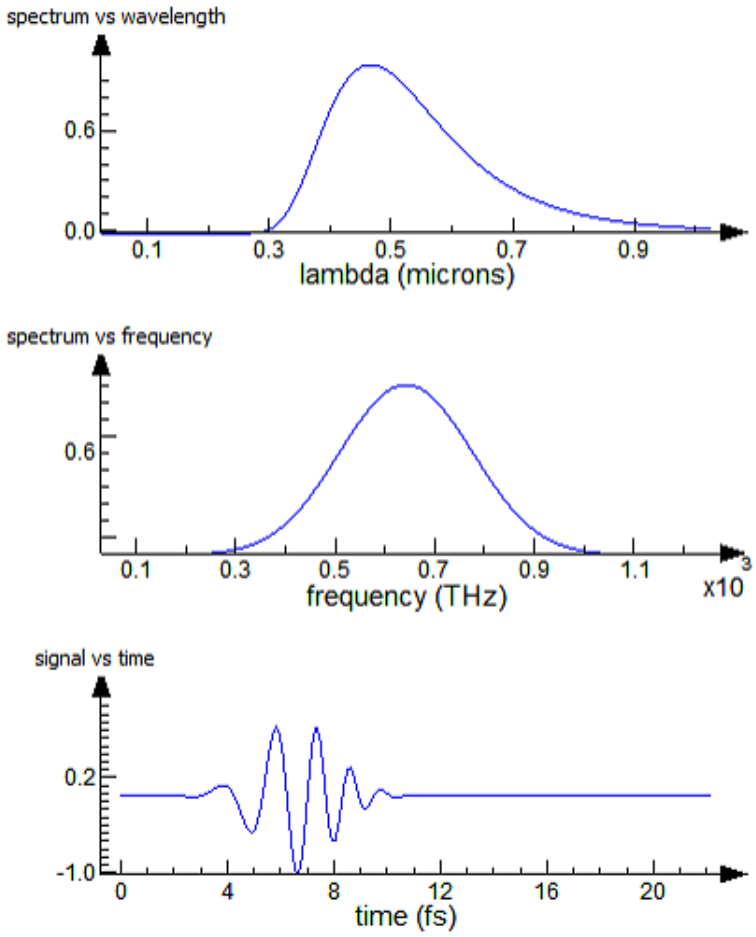

Figure 3.7: Plots of the widefield light source spectrum in terms of wavelength and frequency respectively and representation of the source pulse in time.

artificial absorbing layers capable of minimize the reflections on their surface. This choices were made accordingly to reference [35].

3.2.4.3 2D VS 3D Simulations

In many FDTD simulations it is possible to obtain the same results, or at least similar, using 2D simulations instead of 3D. The motivation for this relies on the fact that 3D simulations require much more memory and time and often they are impossible to perform with a standard standalone high-performance computing workstation as of 2020.

In case of this work the geometries were impossible to be fully simulated using 3D simulations (even when they were possible it was at a very low precision, making them useless) since we didn't have enough computational resources, which did motivate us to evaluate the possibility of using 2D simulation regions instead.

In order to assess the validity of 2D FDTD simulations for our kind of systems,

we created a smaller 3D geometry (smaller enough to be computable at a fairly accuracy) analogous to a cantilever profile, then we transposed that geometry to a 2D equivalent and the results of absorbed power in a gold layer were compared. It was created a 3D rectangle with a 1 x 1 μm of base, composed of a 70 nm gold layer and a 430 nm silicon nitride layer (similar to PNP-TR cantilever profile), which is represented in figure 3.8. The x and y spans were set to 1 μm and the z span was set to 4 μm. The plane wave source was placed 2 μm below the interface between the two layers. The whole simulation region contains water. The x and y directions boundaries were set to be periodic and the Z direction boundaries to be PML (according to section 3.2.4.2).

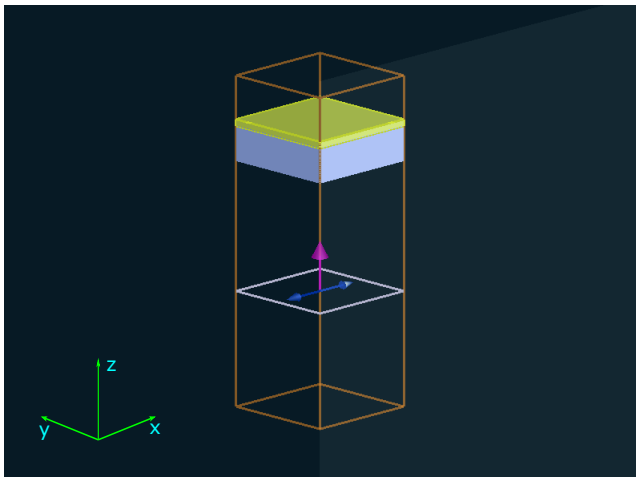

Figure 3.8: 3D optical simulation region perspective view. The source is represented by the empty white rectangle, the direction of light propagation by the pink arrow and the electric field direction by the blue arrows.

Since we are dealing with a plane wave and x and y periodic boundaries, our symmetry suggests that we can simulate the same phenomena considering whether x or y direction as being infinite, allowing us to transpose this geometry to a 2D geometry in a plane parallel whether to xz or yz planes.
In order to transpose the 3D geometry to an equivalent 2D simulation it was created a 2D simulation of a plane profile parallel to the xz plane in the original simulation. It should be noted that the z coordinate in the 3D simulation has a correspondence with the y coordinate in the 2D simulation (the software takes the z coordinate has being infinite *cf.* section 2.2).
The 2D simulation was composed by two rectangular layers with 1 μm of length: a 70 nm gold layer and a 430 nm silicon nitride layer as well and it is presented on the figure 3.9. The x span was set to 1 μm and the y span was set to 4 μm. The plane wave source was placed 2 μm below the interface between the two layers. The whole simulation region contains water. The x direction boundaries were

set to be periodic and the y direction boundaries to be PML (according to section 3.2.4.2).

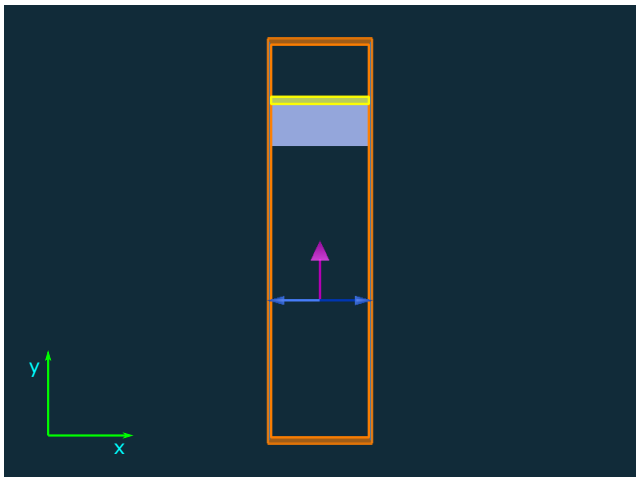

Figure 3.9: 2D optical simulation region xy plan view. The direction of light propagation by the pink arrow and the electric field direction by the blue arrows.

A comparison between 2D and 3D approaches was made using a mesh accuracy of 5 (*cf.* section 2.2) since bigger values were not possible to use (due to available computational resources) in the 3D design. The figure 3.10 aims to show the comparison between the two approaches when it comes to evaluate the fraction of power absorbed in the gold coatings.

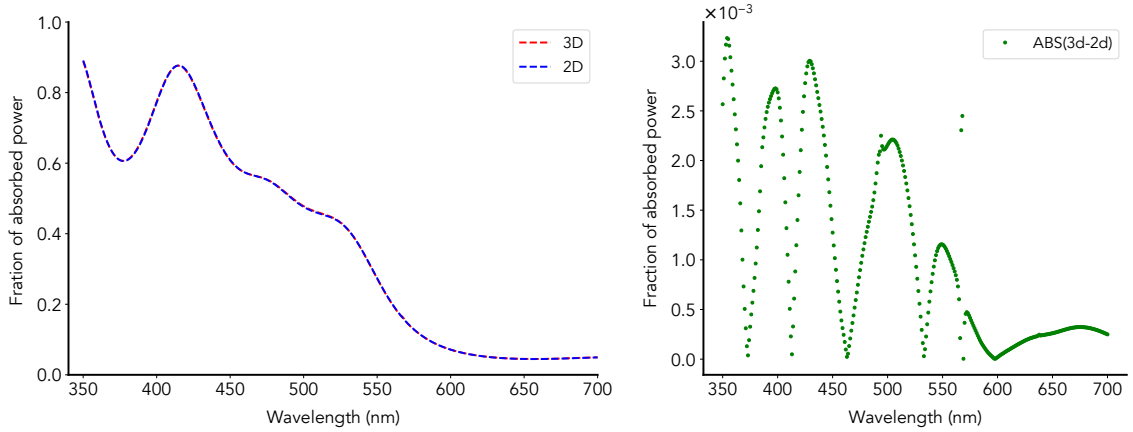

Figure 3.10: Comparison of the gold light absorption between the 2D and the 3D approaches. On the left side are plotted the results for 3D (red) and 2D (blue) and on the right side is plotted the absolute value of the difference between both results.

As one can see in figure 3.10 the results of the two approaches are almost equal and cannot be distinguished, the right side plot shows that the biggest absolute

difference on fraction of absorbed power between the two approaches is approximately 0.0035 (or 0.35%) which indicates that using 2D approaches instead carries a very small trade off on results.
This analysis has shown that we can use a 2D approach instead of 3D considering a plane with the thickness and length profiles of the cantilevers.

3.2.4.4 Geometry for PNP-TR cantilevers

In Miranda et al.[1] publication, the PNP-TR type 1 cantilever was treated as a 3D rectangle with a base area of 1350 μm^2 and a thickness of 500 nm. Then, the assumption of a small width compared with length allowed them to use the Timoshenko's bi-metal strip model (a 2D model that describes the deflection of a bi-metallic strip submitted to temperature increase, presented in appendix A) in order to approximate the temperature with the measured depletion.
For this study it was created a 2D simulation region, with the dimensions of 100×4 μm, a 70 nm gold and a 430 nm silicon nitride layers, a water background and a plane wave, propagating in y-direction, that expands through all x-direction. This geometry is shown in figure 3.11.

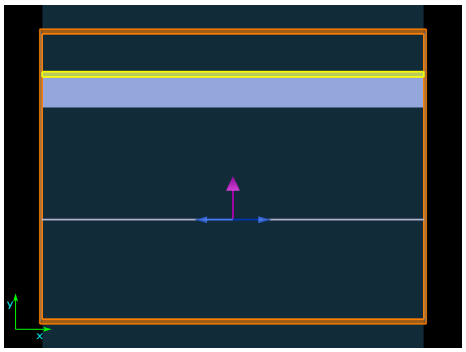

Figure 3.11: Optical simulation geometry for a PNP-TR type 1 cantilever. The orange box represents the simulation region, that is filled with water, the yellow rectangle is the gold layer and below is the silicon nitride layer. The pink arrow indicates the direction of light propagation and the blue ones the direction of the electric field.

3.2.4.5 Convergence testing for PNP-TR cantilevers

A convergence testing was made increasing the mesh accuracy, as it is explained in the convergence testing section (3.2.3), in order to evaluate if the obtained results are arbitrary or far away from what is expected from an higher precision FDTD simulation of this system.
The figure 3.12 summarizes the results of the convergence testing process, it

illustrates the results for each mesh accuracy in a plot and the respective $\Delta\sigma$ values in another plot.

The biggest differences between the results occur in the smaller wavelength region which is expected since smaller wavelengths are more sensitive to changes in geometry (changes in mesh step size in our case). Convergence testing indicates that in fact the results converge, and using mesh accuracy values bigger than 5 leads to a change in values of 0.3% or less (in average over all wavelengths), which indicates that a value of 5 for mesh accuracy is enough in this case, since higher mesh accuracy values don't lead to significant changes in the final results.

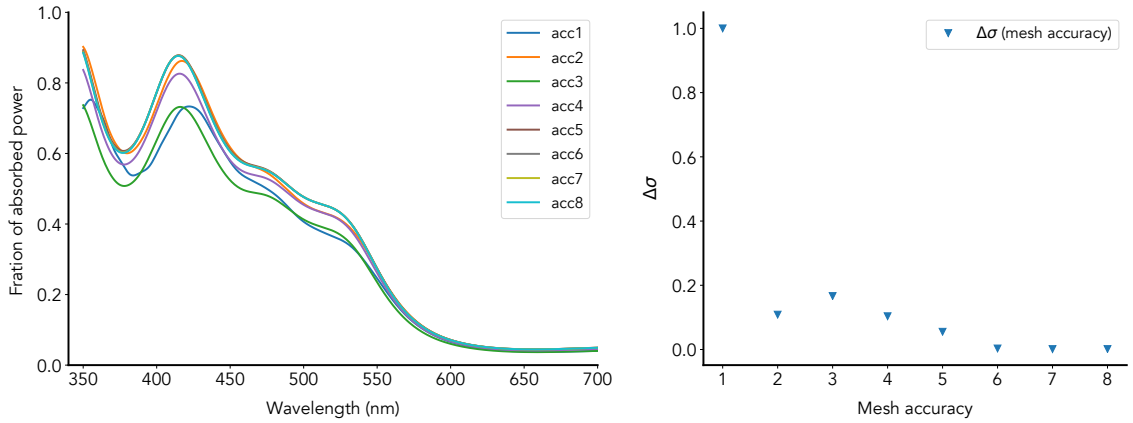

Figure 3.12: Convergence testing of PNP-TR cantilever 2D simulation. Plot of the fraction of absorbed power vs wavelength for mesh accuracy values from 1 to 8 [left]. Plot of the $\Delta\sigma$ values vs mesh accuracy [right].

3.2.4.6 Geometry for qp-BioAc cantilevers

It was created a 2D optical simulation for each qp-BioAc cantilever type. Each simulation region has got the length of respective cantilever and is composed by a plane wave source, a 400 nm thickness silica layer, a 60 nm gold layer and a water background.
In figure 3.13 one can find the optical simulation's geometry for each qp-BioAc cantilever type.
Since it were used periodic boundary conditions for the y-directions boundaries it is required that the advanced power absorbed analysis group has got coincident boundaries with the simulation region y-direction boundaries[8].
It should be noted that since the gold coatings do not cover the entire simulation regions (in the y-direction) the advanced power absorbed analysis groups are measuring some absorption in the water which can be completely neglected due to the very small values of the imaginary part of the water's permitivity, as was stated before in the materials sections (3.2.1).

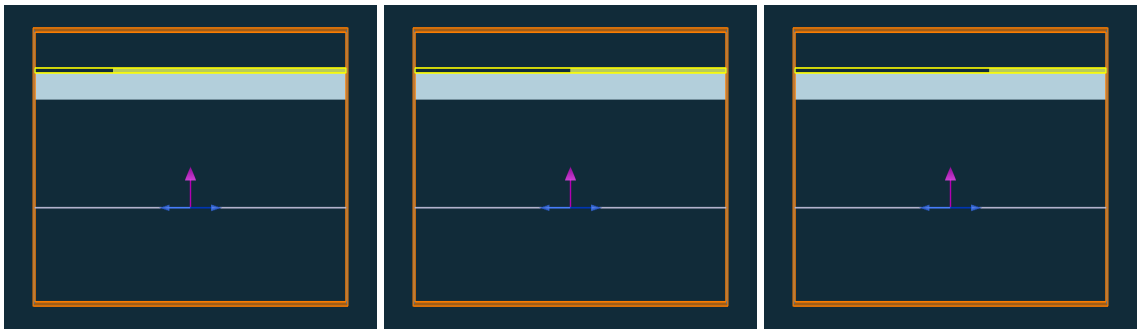

Figure 3.13: qp-BioAc cantilever's optical simulations geometries. CB1, CB2 and CB3 cantilevers are shown from left to right respectively. The orange boxes represent the simulation regions, which are filled with water, the yellow rectangles are the gold layer and below these are the SiO2 layers. The pink arrows indicate the direction of light propagation and the blue ones the directions of the electric fields. The yellow lines represent the advanced power absorbed analysis groups whose y-direction boundaries should be coincident with the simulation region y-direction boundaries.

3.2.4.7 Convergence Testing for qp-BioAc cantilevers

A convergence testing for each qp-BioAc cantilever was made. The figures 3.14 and 3.15 show the fraction of absorbed power in terms of wavelength for each mesh accuracy value and the plot of $\Delta\sigma$ values in terms mesh accuracy, respectively, for each cantilever type.

[8]This information is provided by the power absorbed analysis group script in the software

As expected, the results are very similar for every cantilever type which indicates that in this case the differences in fraction of absorbed power occur due to the fact that for each cantilever there is a different proportion between the total surface area and the gold coating's surface area (this proportion is expressed in the differences in length between the three cantilevers).
The convergence for the three cantilevers is almost equal which reveals the consistency of this approach for these geometries. A different behaviour of the convergence for each cantilever would reveal geometry related errors.

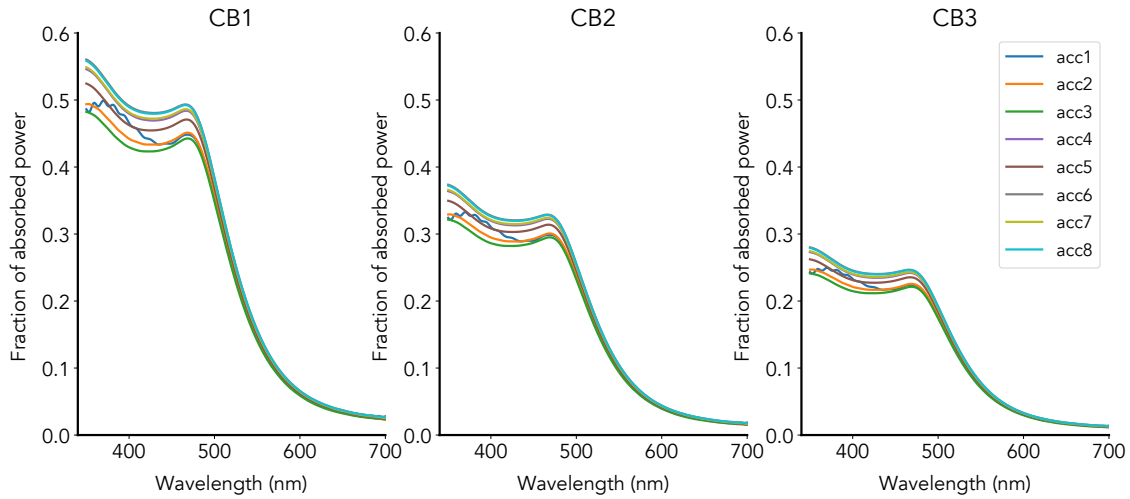

Figure 3.14: Fraction of absorbed power vs wavelength for mesh accuracy values from 1 to 8, for widefield illumination 2D optical simulations of qp-BioAc cantilevers.

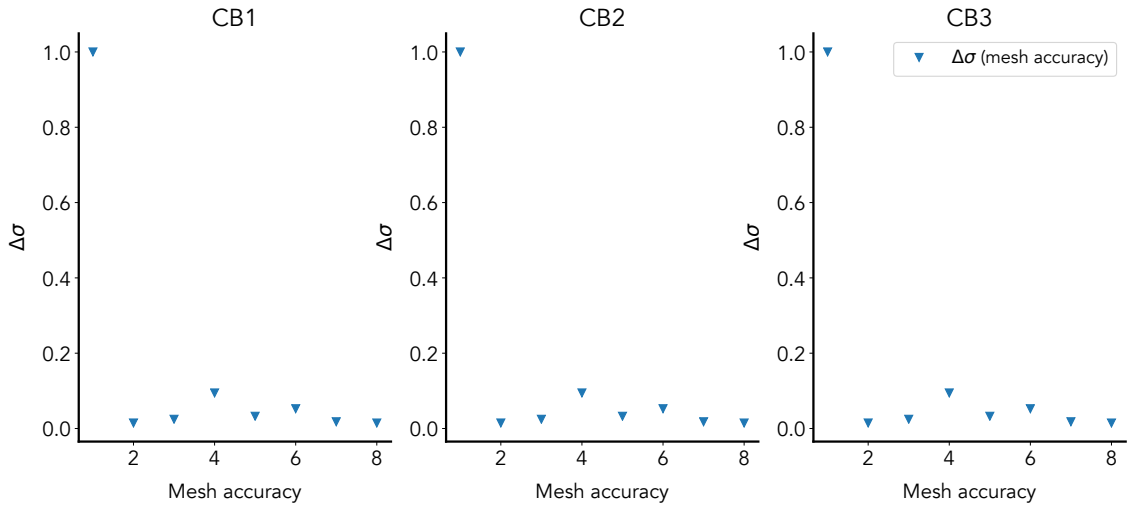

Figure 3.15: $\Delta\sigma$ vs mesh accuracy plots for widefield illumination 2D optical simulations of qp-BioAc cantilevers.

3.2.5 Confocal illumination optical simulations

In confocal illumination optical microscopy set-ups the light is concentrated in a very small spot which illuminates the sample, then the resultant fluorescence is filtered by a pinhole before detection in order to achieve optical sectioning.
Nowadays the confocal spots are achieved using high numerical-aperture lens and can have diameters rounding 250 nm (which is the value we use in our simulations).
In the confocal illumination optical simulations the gold coating's absorption profiles are acquired (the fraction of source power that is absorbed in each unitary cell) for different vertical positions of the confocal spot and different wavelengths. Instead of acquiring the absorbed power for a large broadband, these simulations acquire the absorption data for a single wavelength which allows it to be exported directly to the HEAT solver as an heat source. This procedure is possible in this case because we are using a 3D approach and a geometry that is compatible with the thermal simulation's geometries.

3.2.5.1 Source

In the simulations the confocal spot is created by a Gaussian beam source which defines a beam whose amplitude in each cross-section is defined by a Gaussian envelope with the width defined by the cross-section's diameter.
At very high numerical apertures the image field requires vectorial calculation of the electromagnetic field [36, 37]. Here we are considering a Gaussian approximation of a focused beam, which represents a two-dimensional electromagnetic approximation of the full vectorial solution aforementioned, valid for all but the very highest values of numerical apertures available in biological microscopy. However it remains the best choice in simulating confocal spots.
The source was placed 1 μm below the interface between the gold coating and the cantilever (the source position in our case is not so relevant since we can specify the position of the beam waist in the simulation region) and the beam waist was set to be at the following positions: 0, 3.5 and 7 μm below the beginning of the gold coating in the direction of the light's propagation (z-direction).
Every vertical position of the confocal spot is adressed in a separate simulation. The same happens with the wavelengths (405, 488, 532 and 633 nm).

3.2.5.2 Boundary conditions

The confocal illumination optical simulations were performed in 3D which is translated into a high amount of computational power and time consumption comparing to the wide-field simulations, performed in a 2D approach.
Luckily in our case these issues can be attenuated taking advantage of the available boundary conditions.
The polarization of the Gaussian source was set to be in the x-direction. For our case, following the reference [38], we can use symmetric and anti-symmetric boundaries since the electromagnetic fields have 2 planes of symmetry (the 2 planes defined by the conditions x=0 and y=0) which pass trough the middle of simulation region. Following this idea, since the source polarization is normal to the x boundaries, these were set to be anti-symmetric. The y boundaries were set to be symmetric since the source polarization is tangential to these boundaries. The z boundary condition was set to be PML (similar to widefield illumination optical simulations).
In our case, since we used symetric/anti-symetric boundaries, this procedure allowed us to reduce in 4 times the computational time and memory required.

3.2.5.3 Simulation geometry for PNP-TR and qpBioAc cantilevers

The optical simulations for confocal illumination of PNP-TR and qp-BioAc cantilevers were performed in 20 X 20 X 1.5 μm simulation regions filled with water, displayed in the figure 3.16. These dimensions were selected in order to allow us to simulate different positions of the confocal spot, without loosing source power (since the beam diameter increases with the distance from the waist), when it is farther from the interface between the gold coating and the cantilever (z=0 position).
The simulation regions for each cantilever were composed by two rectangular layers: a 20 X 20 X 0.07 μm gold layer and a 20 X 20 X 0.43 μm silicon nitride layer for PNP-TR cantilevers, and a 20 X 20 X 0.06 μm gold layer and a 20 X 20 X 0.4 μm silica layer for qp-BioAc cantilevers.
The source was placed 1 μm (z=-1) below the beginning of the gold coating and in the center considering x and y directions (x=0 and y=0).
It should be mentioned that for some cantilevers this surface area may be bigger than the real surface area illuminated by the beam, however this is corrected when the absorption profiles are imported as heat sources in the HEAT solver where the geometries of each cantilever are better explicit, since the absorption profiles can be imported in a specific solid of the thermal simulation, which is the

gold coating in our case.

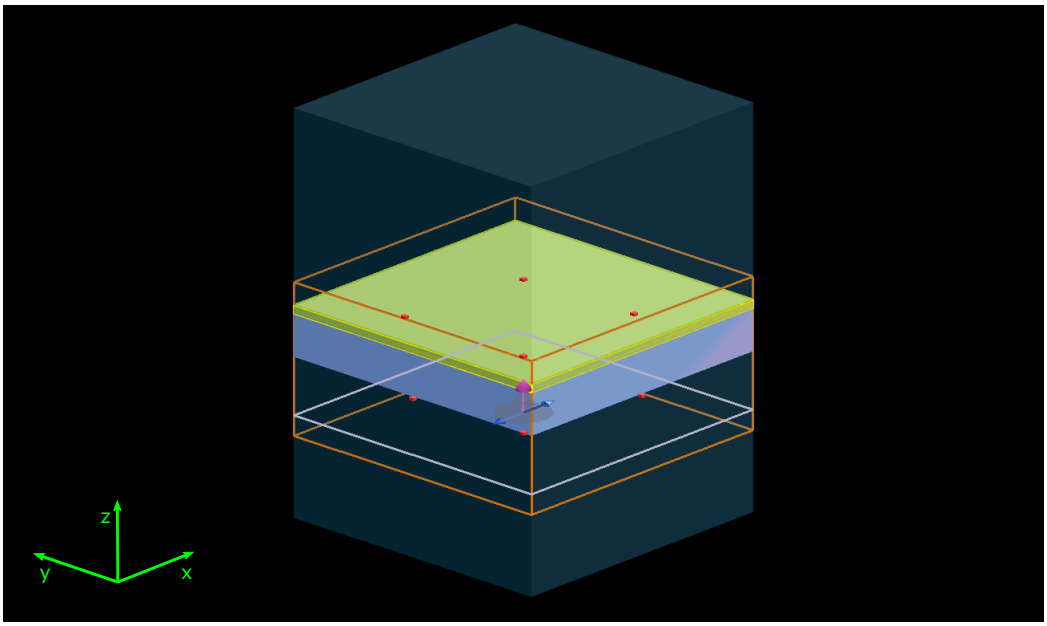

Figure 3.16: Geometry for confocal simulations. Herein the geometry for PNP-TR, which is similar to the geometry for qp-BioAc, is represented. The pink arrow indicates the propagation direction of the beam and the blue arrows represent the source polarization direction. The other elements in the image are analogous to the objects present in the images provided above regarding other simulations.

3.2.5.4 Convergence testing for PNP-TR and qp-BioAc cantilevers

In case of confocal illumination, since every single simulation has only one wavelength, the sum in equation 3.1 reduces to one term. In this approach, we use the power absorbed per unit volume in each cell instead of total power, however the convergence testing is performed using the value of fraction of total power absorbed, as was done with the wide-field simulations.

The fraction of total power absorbed was acquired for each mesh accuracy value from 1 to 5 (the highest value we were able to simulate with our resources) for 488 and 532 nm and from 1 to 4 for 405 and 633 nm. In the case of the last 2 wavelengths it was impossible to go further in terms of mesh accuracy, which happens because Lumerical's conformal mesh technology (*cf.* subsection 2.2.1.3) imposes a very small cell sizes for both wavelengths. In case of 405 nm the small cell size is imposed by the small wavelength value, in case of 633 nm it is imposed by the high value of relative gold's real part of electrical permitivity absolute value for that wavelength. This can be confirmed in the materials sub-subsection 3.2.1.

The beam waist was considered to be at at z=0 vertical position. The convergence testing results for both PNP-TR and qp-BioAc cantilevers are presented, respectively, in figures 3.17 and 3.18.

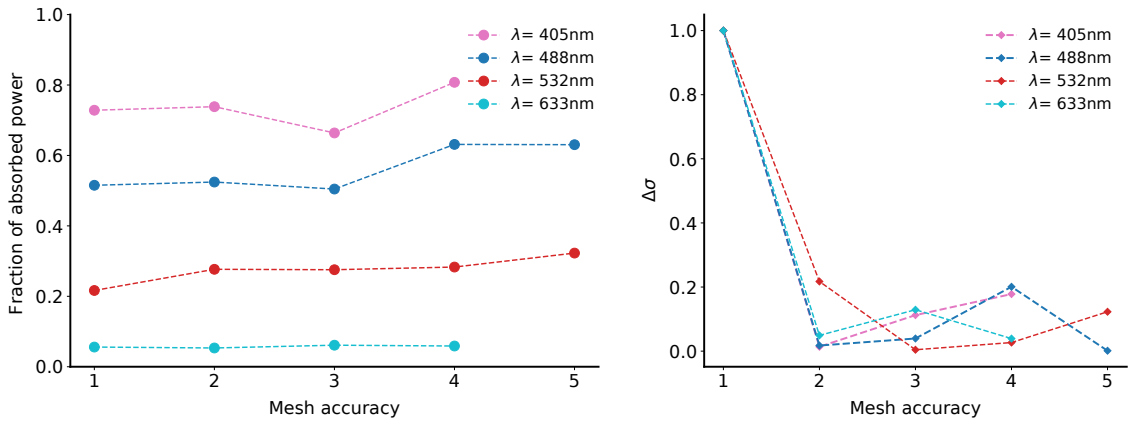

Figure 3.17: Confocal illumination optical simulations convergence testing for PNP-TR cantilevers. Fraction of absorbed power vs wavelength for mesh accuracy values from 1 to 5 for confocal illumination (405/488/532/633 nm) considering the beam waist on the beginning of a PNP-TR cantilever's gold coating [left] and $\Delta\sigma$ calculation for those values [right].

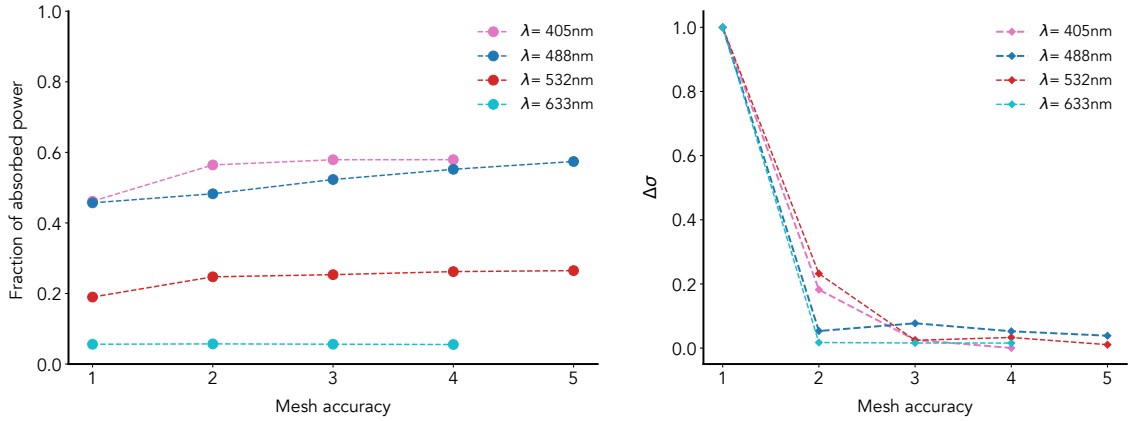

Figure 3.18: Confocal illumination optical simulations convergence testing for qp-BioAc cantilevers. Fraction of absorbed power vs wavelength for mesh accuracy values from 1 to 5 for confocal illumination (405/488/532/633 nm) considering the beam waist on the beginning of a qp-BioAc cantilever's gold coating [left] and $\Delta\sigma$ calculation for those values [right].

In case of PNP-TR cantilevers, although we have some error for 405 and 532 nm and a big change in values for 488 nm with a mesh accuracy value of 4, we can consider that we have some convergence or at least more than enough for our degree of precision. It can be estimated an error of: 18% for 405 nm, 0.13% for 488 nm, 12% for 532 nm and 3.9% for 633 nm.

In case of qp-BioAc cantilevers, it can be verified that we have a convergence of the results for both wavelengths and errors of: 0.03% for 405nm, 4% for 488 nm, 1% for 532 nm and 1.6% for 633nm.

3.3 Thermal simulations

Thermal simulations were performed for PNP-TR type 1 and all qp-BioAc cantilevers. The PNP-TR type 2 cantilevers were not simulated since they would require a much bigger simulation region impossible to simulate with our resources, however the results are expected to be analogous, since they have got similar geometries.
The different cantilever geometries were submitted to different heat sources which were created with the information provided by the optical simulations.
In this section it is comprised all the information needed to present and sustain the choices made and the work done regarding thermal simulations that were performed in order to evaluate the temperature increase on both cantilevers caused by the different illumination set-ups.
It starts by presenting the materials and heat sources. Then it contains a detailed description of the geometric model for each cantilever followed by a description of the simulation regions and boundary conditions. This section finishes presenting an overview of the thermal simulations performed.

3.3.1 Materials

The required material properties for heat transport simulations are: density (kg/m^3), specific heat (J/kg.K) and thermal conductivity (W/m.k). In our case the required materials were water, gold, silicon nitride (PNP-TR cantilevers) and silica (qp-BIoAc cantilevers). On the next list one can find the respective simulation material's correspondence:

- **Gold**: Au (Gold) - CRC
- **Silicon nitride**: Si_3N_4 (Silicon Nitride) - Sze
- **Silica**: SiO_2 (Glass) - Sze;
- **Water**: The HEAT solver aims to simulate the heat propagation in solids, consequently it has no data for water. Anyway it was created a material (solid) with the following characteristics:

- Density: 996 kg/m^3;
- Specific heat 4178 J/kg.K;
- Thermal conductivity 0.6 W/m.k.

The water material was created following the reference [39] and in order to simulate better a liquid it was created a convection boundary condition between gold and water.

3.3.2 Heat sources

In order to evaluate the temperature increase caused by the power absorption on the gold coating, heat sources need to be defined in the thermal simulations. These sources were defined in two different ways according to the illumination schemes (widefield and confocal).
For the widefield illumination scheme it is manually defined a uniform heat source (covering all the gold coating) with the power provided by the product of the fraction of power that is absorbed for a specific wavelength with the total power incident on the cantilever's surface. This happens because the optical simulations are performed in 2D and for a broadband of wavelengths (each wavelengths defines a different absorption profile) and the thermal simulations are in 3D, which means that the absorption profile provided by the optical simulations cannot be imported directly into thermal simulations.
In case of confocal illumination it is defined a heat source based on the absorption profile collected for each wavelength with the confocal spot at the different simulated positions. One should remember (*cf.*3.2.5) that this absorption profile is collected in a 20X20X0.07 μm volume which, in some cases, may have a bigger surface than the gold coating's surface, anyway the HEAT solver allow us to define the absorption profile to act as an heat source just on the gold coating which prevents some absorption calculated on gold's 20X20X0.07 μm volume to act wrongly as an heat source in water *cf.* figures 3.16 and 3.19.

3.3.3 Geometries for each cantilever

As expected, the sizes of each cantilever piece of the same model are different due to the fabrication process, so the values used in the models presented next are the nominal values. In this project the manufacturers of each cantilever model were contacted in order to create a more realistic geometry since the information available in the companies websites (references [32, 33]) was not enough.

3.3.3.1 PNP-TR cantilevers

Two polygon layers (a 0.07 μm thickness gold layer and a 0.43 μm thickness silicon nitride layer) were created to model the shape of PNP-TR cantilevers (*cf.* 3.1.1). The polygons were created specifying the x and y coordinates of the vertices. The figure 3.19 presents the PNP-TR model geometry.

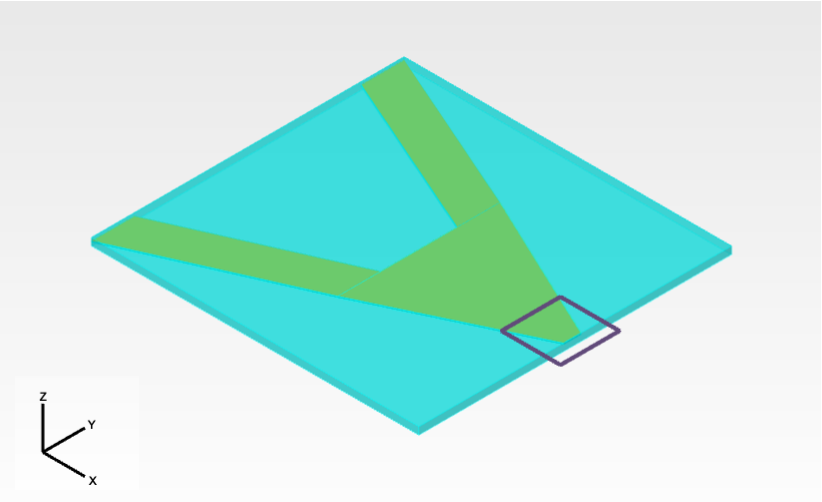

Figure 3.19: Thermal simulation geometry for PNP-TR cantilevers. In the image it is possible to see the gold coating (yellow) and right bellow it is the cantilever's silicon nitride layer. The blue rectangle represents the surrounding water and the purple square represents the heat source (in case of confocal illumination, otherwise the source would be on the whole gold coating).

The (x,y) coordinates of the polygon's vertices (respecting the figure's 3.19 coordinate system) in μm are: (0,53), (0,38.5), (58,27.5), (58,-27.5), (0,-38.5), (0,-53), (110,-3), (110,3). This results in a surface area of 2332 μm ^{2} given by the shoelace algorithm[9].

A linear temperature monitor[10] is used in order to evaluate the cantilever's temperature profile in the x-direction. This monitor is placed in the middle of the cantilever in terms of directions y and z and it goes from x=58 to x=110 μm (which can be regarded in the image as the triangular part of the polygon).

3.3.3.2 qp-BioAc cantilevers

We modeled the three types of qp-BioAc cantilevers (CB1, CB2 and CB3) which differ in length and width from each other.

Following the information provided by the manufacturer's, the gold coating,

[9] $A = \frac{1}{2}\left|\sum_{i=1}^{n-1} x_i y_{i+1} + x_n y_1 - \sum_{i=1}^{n-1} x_{i+1} y_i - x_1 y_n\right|$ Where A denotes the area and the x_i and y_i stand for the coordinates of each vertex and n the number of vertices.

[10] Evaluate the temperature in each cell in x-direction keeping the y and z coordinates constant.

which aims to cover only the free end of the cantilevers, has got a length of approximately 30 μm.
Two rectangular layers (a 0.06 μm thickness gold layer and a 0.4 thickness SiO_2 layer) were created for each cantilever type, similarly to the previous case. The width and the length of the layers were defined, for every cantilever, accordingly to the subsection 3.1.2 and the length of the gold layers was set to be 30 μm.
The figure 3.20 presents the thermal simulation's geometry for the three types of the qp-BioAc cantilevers.

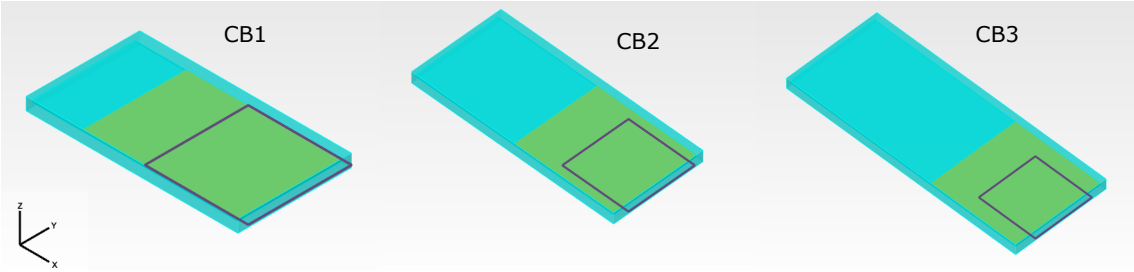

Figure 3.20: Thermal simulation geometry for qp-BioAc cantilevers. As in case of PNP-TR geometry we have the gold coating (yellow) right above the cantilever's silica layer (which is dificult to see due to the surrounding water which is represented by the blue rectangle). The purple rectangle represents the confocal heat source which in case of wide field illumination can be changed by an uniform heat source covering the whole gold coating.

In case of qp-BioAc cantilevers we have a gold coating surface area of: 600, 750, 900 μm^2 for CB1, CB2 and CB3 cantilevers respectively.
As in the case of PNP-TR cantilevers, it was placed a linear x-direction temperature monitor in the middle of the gold coating in terms of y and z directions.

3.3.4 Simulation region and boundary conditions

As mentioned in the theoretical subsection about thermal simulations (2.2.2), one has to set the temperature at a given point (or plane) through fixed temperature boundary conditions. Since we are simulating live cell imaging environments we should set the ambient temperature to be at 310.15 K (37ºC) which is done forcing a plane inside the water to be at that temperature (thermal equilibrium). In our case, since we want to evaluate the temperature raise in the gold coating caused by the different illumination schemes and the cantilever's tips (functional part of the cantilevers) and the bodies being analyzed by an AFM are situated in the lower surface, the fixed temperature (310.15 K) boundary was set to be the lower z-direction simulation region limit.

The simulation region's x-direction and y-direction spans, which were kept constant during all simulations, for each cantilever are listed in table 3.3.

Table 3.3: x and y directions simulation region's spans in micrometers.

	x span (μm)	y span (μm)
PNP-TR	111	106
CB1	41	22
CB2	61	27
CB3	81	32

In x-direction the simulation regions for all cantilevers begin at the cantilever's beginning and end 1 μm away from the cantilevers free ending.
In y-direction, in case of rectangular cantilevers (qp-BioAc), the simulation regions begin and end 1 μm away from the cantilever's limits. In case of PNP-TR the simulation region extends 53 μm from the origin for each side in y direction which is coincident with the cantilever's vertices with the respective (x,y) coordinates: (0,53) and (0,-53). For better visualization of this description one can consider the geometry images for each cantilever type (figures 3.19 and 3.20).
The upper limit (in z-direction) of the simulation regions where set to be 1μm away from the cantilever's up surface.
In case the z-direction lower limit, which is the one where it was defined to occur thermal equilibrium, the distance was varied in order to evaluate two different equilibrium scenarios. This was done due to the lack of experimental data regarding this topic which would be able to better sustain the choice of the fixed temperature thermal boundary conditions.
Although there is no experimental data regarding this, one needs to set a plane where the temperature is equal to the environment's temperature which can happen a few nanometers away from the cantilevers or many micrometers. In case of PNP-TR cantilevers we have a very huge simulation region which makes it impossible for us to extend it further in z-direction (downwards). The maximum distance from the cantilevers down surface that we were able to evaluate was 9 μm. Considering this limitation the maximum temperature reached on this type of cantilevers was evaluated considering an equilibrium distance from 1 to 9 μm from the cantilever's down surface (considering one confocal and one widefield illumination schemes. These results are plotted in the figure 3.21 and presented in table 3.4. They were collected considering a 1 mW 405 nm laser beam focused on the gold coating (confocal illumination) and considering an incident 560 nm widefield illumination with 302 μW (explained further in the next subsection 3.3.5). The result's behaviour is expected to be analogous for the rest of the illumination

schemes and cantilevers.

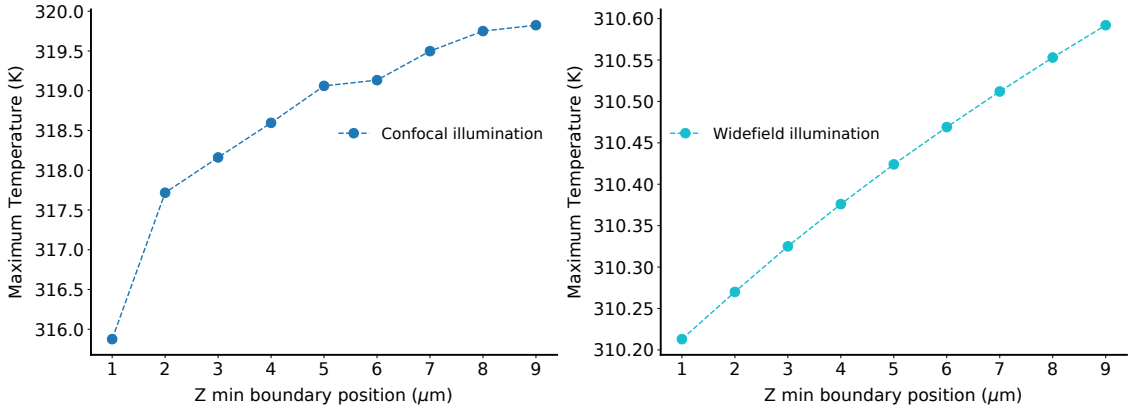

Figure 3.21: Maximum temperature reached for PNP-TR cantilevers considering the thermal equilibrium at a distance from 1 to 9 μm below its down surface.

Table 3.4: Maximum temperature reached for PNP-TR cantilevers considering the thermal equilibrium at a distance from 1 to 9 μm below its down surface: table containing the results plotted on figure. 3.21

Illumination scheme\Z min boundary position (μm)	1	2	3	4	5	6	7	8	9
Confocal illumination	315.876	317.717	318.161	318.596	319.061	319.133	319.498	319.750	319.824
Widefield illumination	310.213	310.270	310.325	310.376	310.424	310.469	310.512	310.553	310.592

As one can confirm the temperature changes between the different executions decrease highly with the increasing of the lower z-direction boundary, in case of confocal illumination and it is roughly constant in case of widefield illumination. Any other focusing position below the gold coating should be considered as an intermediate situation between the widefield illumination and the confocal illumination directly focused in the gold coating.
This study was made to better understand the results behaviour when it comes to increase the distance where the thermal equilibrium occurs, since we could not perform simulations considering higher Zmin boundary positions.

3.3.5 Performed Simulations overview

Following the previous content we now present an overview regarding the thermal simulations performed which results are presented in the next chapter.
In case of widefield illumination, it was just evaluated the set-up presented by Miranda et al. [1] which was one of the big inspirations on this topic. Nonetheless other experimental schemes can be tested if one knows how much of the light power is incident of the AFM cantilever (which can be approximated, considering the lens field of view and the cantilever's area, following the article mentioned

before).
As one can confirm in the subsection 3.3.3 the PNP-TR cantilever has, approximately, an area of 2332 μm^2 (contrary to the first approximation made by Miranda et al. this approximation is based on more specific geometric information provided by the cantilever's manufacturer) which for that set-up gives an incident power on the cantilever down surface of 302 μW. For the same optical set-up we have for CB1, CB2 and CB3 cantilevers an incident power of: 78, 97 and 117 μW respectively.
Following the widefield illumination optical simulations we have, for a wavelength of 560 nm, a power absorbed fraction of 0.2. This factor is multiplied by the incident power in the definition of the uniform heat source.
The following list comprises all the thermal simulations performed considering a widefield illumination (8 in total). Much more simulations were performed (for testing purposes) anyway these are the ones considered to be relevant to be contemplated on the results.

- **PNP-TR cantilever:** using an uniform heat source power of 60.4 μW (0.2*302 μW) and considering the following thermal equilibrium distances: 1 and 9 μm;
- **CB1 cantilever:** using an uniform heat source power of 15.6 μW (0.2*78 μW) and considering the following thermal equilibrium distances: 1 and 9 μm;
- **CB2 cantilever:** using an uniform heat source power of 19.4 μW (0.2*97 μW) and considering the following thermal equilibrium distances: 1 and 9 μm;
- **CB3 cantilever:** using an uniform heat source power of 23.4 μW (0.2*117 μW) and considering the following thermal equilibrium distances: 1 and 9 μm.

As already presented, in case of confocal illumination simulations with four different wavelengths were performed, considering the confocal spot at three different vertical positions and a power of 1 mW. The following list comprises that information.

- **PNP-TR cantilever:** Considering a 1 mW confocal laser spot with the respective wavelengths: 405, 488, 532 and 633 nm. These spots were considered to be focusing on the respective distances below the gold coating: 0, 3.5 and

7 μm. For each case it was considered a thermal equilibrium at 1 and 9 μm. Which gives a total of 24 thermal simulations for PNP-TR cantilevers.

- **CB1 cantilever:** Considering a 1 mW confocal laser spot with the respective wavelengths: 405, 488, 532 and 633 nm. These spots were considered to be focusing on the respective distances below the gold coating: 0, 3.5 and 7 μm. For each case it was considered a thermal equilibrium at 1 and 9 μm. Which gives a total of 24 thermal simulations for CB1 cantilevers;
- **CB2 cantilever:** Considering a 1 mW confocal laser spot with the respective wavelengths: 405, 488, 532 and 633 nm. These spots were considered to be focusing on the respective distances below the gold coating: 0, 3.5 and 7 μm. For each case it was considered a thermal equilibrium at 1 and 9 μm. Which gives a total of 24 thermal simulations for CB2 cantilevers;
- **CB3 cantilever:** Considering a 1 mW confocal laser spot with the respective wavelengths: 405, 488, 532 and 633 nm. These spots were considered to be focusing on the respective distances below the gold coating: 0, 3.5 and 7 μm. For each case it was considered a thermal equilibrium at 1 and 9 μm. Which gives a total of 24 thermal simulations for CB3 cantilevers.

In the chapter 4, 104 thermal simulation (8 considering a widefield illumination and 96 considering different confocal illumination schemes) are presented. Thermal simulations considering thermal equilibrium at distances other than 1 or 9 μm were just performed for the specific study presented in 3.3.4, and since they should be regarded as a convergence study, they are not part of the results.

Chapter 4

Results and discussion

In this chapter one will find the presentation and the discussion of the achieved results.
Firstly the widefield illumination results are presented for both PNP-TR and qp-BioAc cantilevers which are followed by the presentation of the confocal illumination results for both cantilevers.
After the results presentation it follows an overview containing the maximum temperature increases reached in the different set-ups and for the different boundary conditions, which enables a better visualization of the differences between all the possibilities.
Finally, the results are discussed.

4.1 Widefield illumination

In this section there are presented the resultant temperature increase linear profiles for the different simulations performed considering a widefield illumination. It is divided by cantilever type.

4.1.1 PNP-TR cantilevers

In figure 4.1 there are presented the resultant temperature increase linear profiles in x-direction measured at the middle of the cantilever's gold coating (in both y and z directions) for a PNP-TR cantilever illuminated with a widefield light source with 560 nm of wavelength and 60.4 μW of total power. These results consider

the two different boundary conditions that were set: fixed 310.15K temperature at 1 and 9 μm below the cantilever's down surface.
It was observed a maximum temperature increase of 0.44 K considering a thermal equilibrium at 9 μm away and and a maximum temperature of 0.06 K considering a thermal equilibrium at 1 μm away.

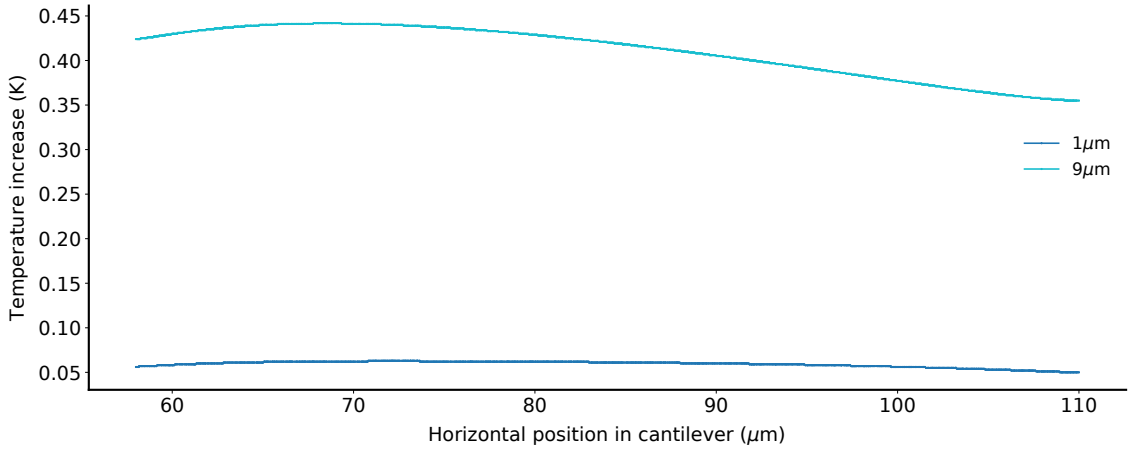

Figure 4.1: Temperature increase linear profile generated by widefield illumination of a PNP-TR type 1 cantilever. linear temperature profile considering the middle of the cantilever's gold coating according to y and z directions. The x values start in 58 μm due to the PNP-TR triangular geometry. The temperature profiles are plotted considering a thermal equilibrium at 1 and 9 μ distances (dark and light blue lines, respectively).

4.1.2 qp-BioAc cantilevers

In figure 4.2 the resultant temperature increase linear profiles in x-direction measured at the middle of the cantilever's gold coating (considering both y and z directions) are presented for qp-BioAc cantilevers (CB1, CB2 and CB3) illuminated with a widefield light source with 560 of wavelength.
The source total powers are 15.6, 19.4, 23.4 μW for CB1, CB2 and CB3 cantilevers respectively (*cf.* 3.3.5) .
These results consider the two different boundary conditions that were set: fixed 310.15K temperature at 1 and 9 μm below the cantilever's down surface.
In case of qp-BioAc we have three different cantilevers (CB1 CB2 and CB3). The gold coating starts at 10, 30 and 50 μ position (x-direction) for CB1, CB2 and CB3 cantilevers respectively and has a length of 30 μm in the three cases. This opens the possibility to represent the temperature profiles for the three cantilevers in the same plot.

Considering a thermal equilibrium at 1μm below the cantilever we have a maximum temperature increase of 0.05 K for the three cantilevers.
Considering a thermal equilibrium at 9μm below the cantilever we have a maximum temperature increase of 0.32 K for CB1 and CB2 and 0.33 K for CB3 cantilevers.

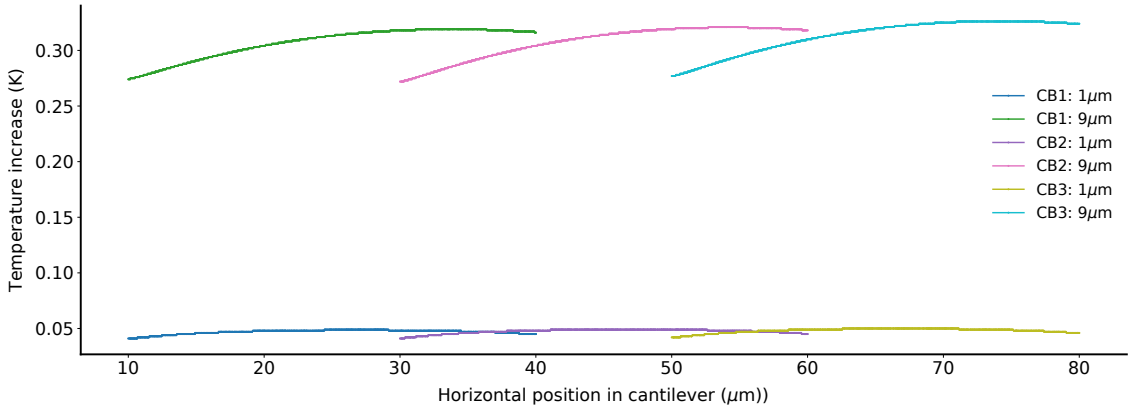

Figure 4.2: Temperature increase linear profile generated by widefield illumination of qp-BioAc cantilevers. linear temperature profile considering the middle of the cantilever's gold coating according to y and z directions. The temperature profiles are plotted considering a thermal equilibrium at 1 and 9 μm for the different cantilever types (green and dark blue lines for CB1, red and purple lines for CB2 and light blue and yellow lines for CB3).

4.2 Confocal illumination

In this section the resultant temperature profiles for the different simulations performed are presented considering a confocal illumination scheme. It is divided by cantilever type.

4.2.1 PNP-TR cantilevers

The linear x-direction temperature profiles generated in PNP-TR cantilevers with a total power of 1mW are presented in the figures 4.3, 4.4, 4.5 and 4.6.
The figures are separated by wavelength (405, 488, 532 and 633 nm) and in each one the temperature profiles are plotted, considering the confocal spot at 0, 3.5 and 7 μm away from the gold coating, and for each of this cases we have the profiles considering a thermal equilibrium at 1 and 9 μm below the cantilever's surface.
In case of a 405 nm light and considering a thermal equilibrium at 1μm below the cantilever we have maximum temperature increases of 5.73, 3.07 and 2.25

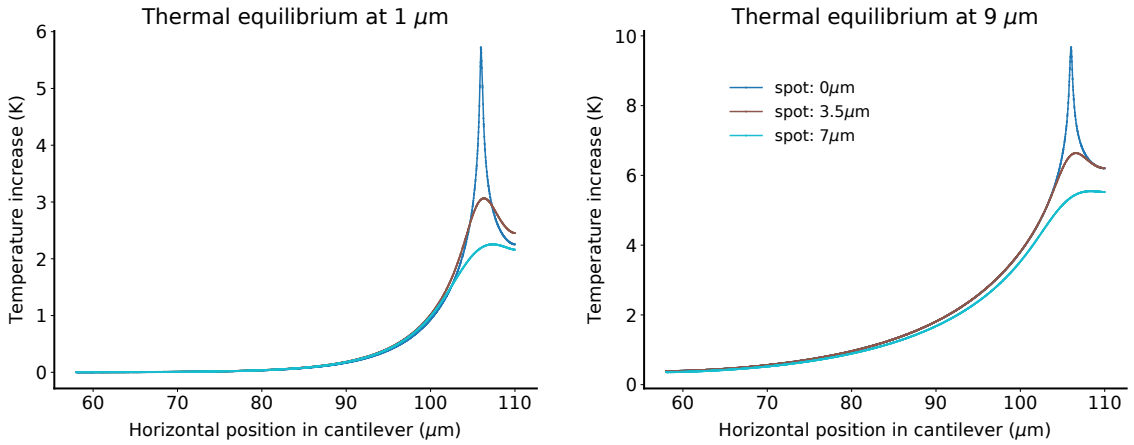

Figure 4.3: Linear x-direction PNP-TR cantilever's temperature profile considering a confocal light source with a wavelength of 405 nm and a total power of 1 mW.

K, for confocal focusing distances of 0, 3.5 and 7 μm respectively. With a thermal equilibrium at 9 μm below the cantilever we have maximum temperature increases of 9.67, 6.64 and 5.55 K, for confocal focusing distances of 0, 3.5 and 7 μm respectively.

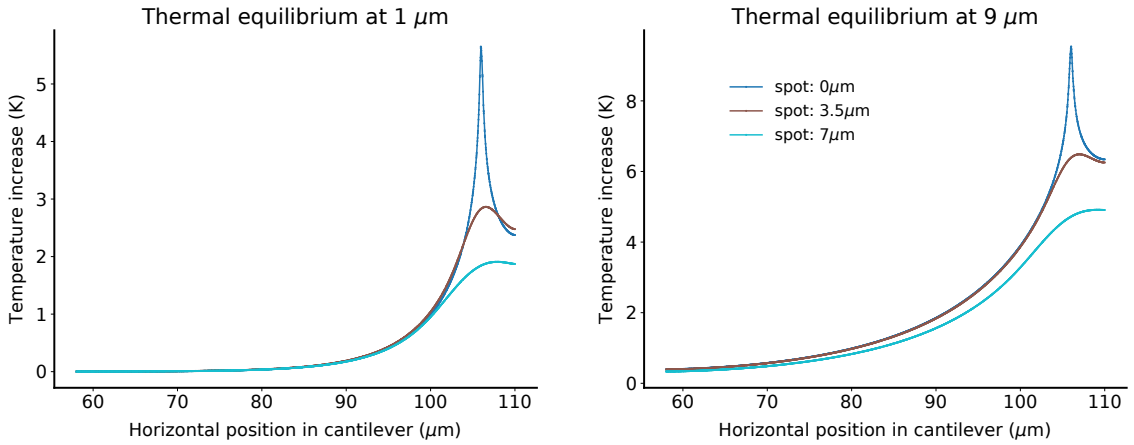

Figure 4.4: Linear x-direction PNP-TR cantilever's temperature profile considering a confocal light source with a wavelength of 488 nm and a total power of 1 mW.

In case of a 488 nm light and considering a thermal equilibrium at 1μm below the cantilever we have maximum temperature increases of 5.65, 2.86 and 1.91 K, for confocal focusing distances of 0, 3.5 and 7 μm respectively. With a thermal equilibrium at 9 μm below the cantilever we have maximum temperatures of 9.55, 6.49 and 4.91 K, for confocal focusing distances of 0, 3.5 and 7 μm respectively. In case of a 532 nm light and considering a thermal equilibrium at 1μm below the cantilever we have maximum temperature increases of 2.7, 1.42 and 1.00

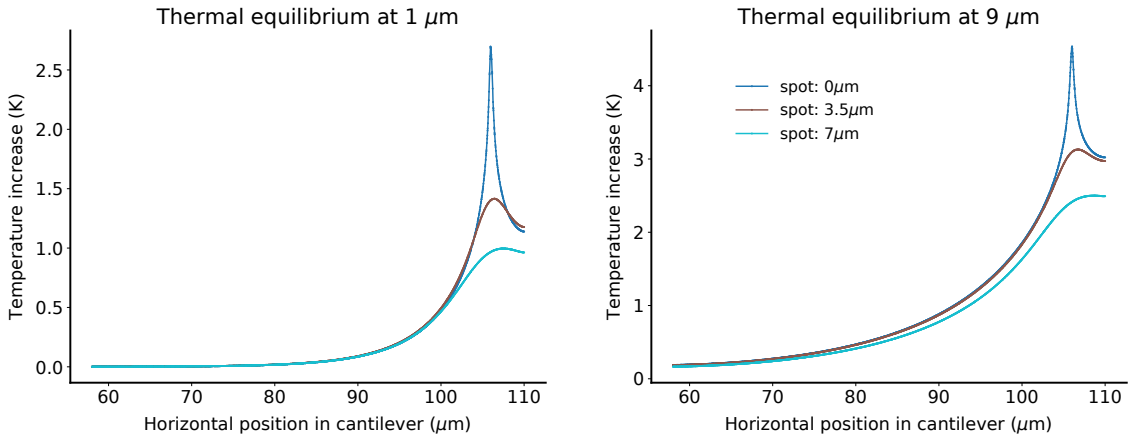

Figure 4.5: Linear x-direction PNP-TR cantilever's temperature increase profile considering a confocal light source with a wavelength of 532 nm and a total power of 1 mW.

K, for confocal focusing distances of 0, 3.5 and 7 μm respectively. With a thermal equilibrium at 9 μm below the cantilever we have maximum temperature increases of 4.54, 3.13 and 2.50 K, for confocal focusing distances of 0, 3.5 and 7 μm respectively.

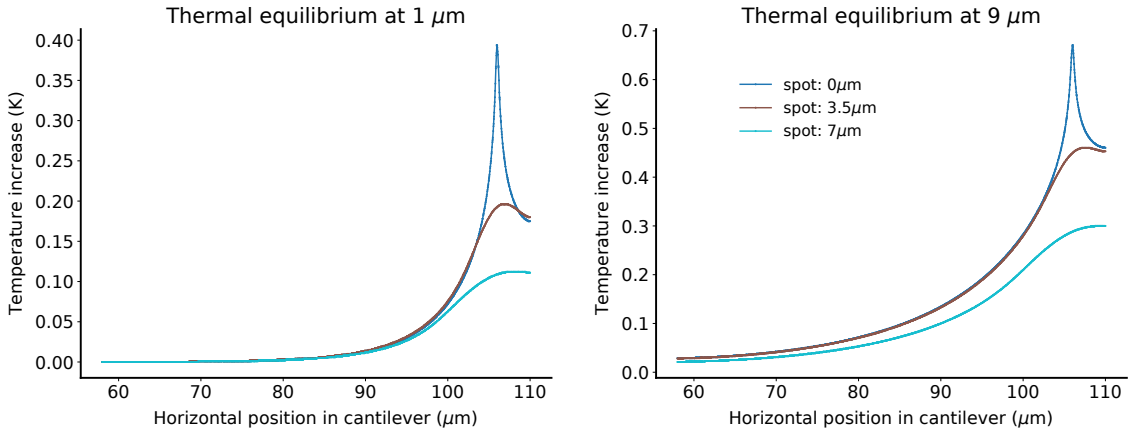

Figure 4.6: Linear x-direction PNP-TR cantilever's temperature increase profile considering a confocal light source with a wavelength of 633 nm and a total power of 1 mW.

Finally in case of a 633 nm light and considering a thermal equilibrium at 1μm below the cantilever we have maximum temperature increases of 0.39, 0.20 and 0.11 K, for confocal focusing distances of 0, 3.5 and 7 μm respectively. With a thermal equilibrium at 9 μm below the cantilever we have maximum temperature increases of 0.67, 0.46 and 0.30 K, for confocal focusing distances of 0, 3.5 and 7 μm respectively.

4.2.2 qp-BioAc cantilevers

The linear x-direction temperature increase profiles generated in qp-BioAc cantilevers with a total power of 1mW are presented in figures 4.7, 4.8, 4.9 and 4.10, which comprise those profiles for the three cantilever types CB1, CB2 and CB3 (similarly to the widefield results section 4.1). There is one figure for each wavelength (405, 488, 532 and 633 nm) containing the temperature increase profiles considering the confocal spot at 0, 3.5 and 7 μm away from the gold coating and considering the two different distances of thermal equilibrium evaluated: 1 and 9 μm below the cantilever.

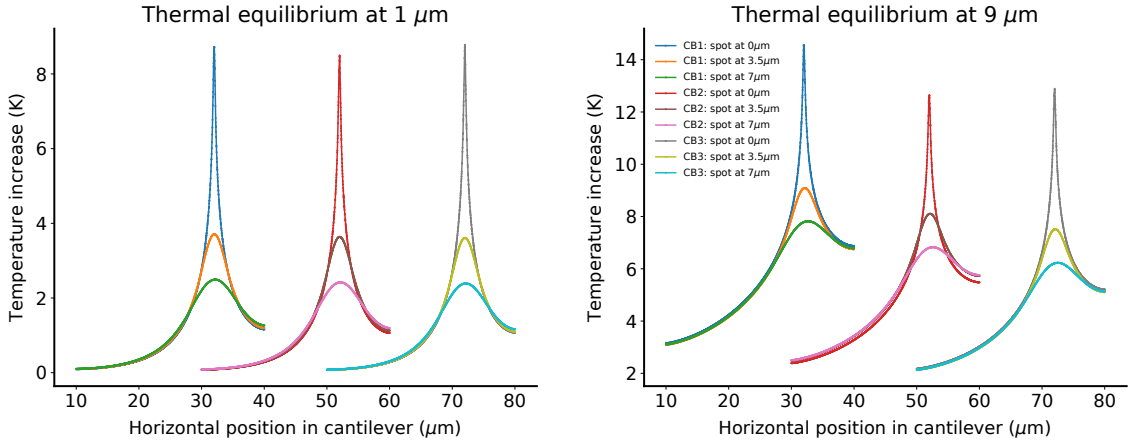

Figure 4.7: Linear x-direction qp-BioAc cantilever's temperature increase profile considering a confocal light source with a wavelength of 405 nm and a total power of 1 mW.

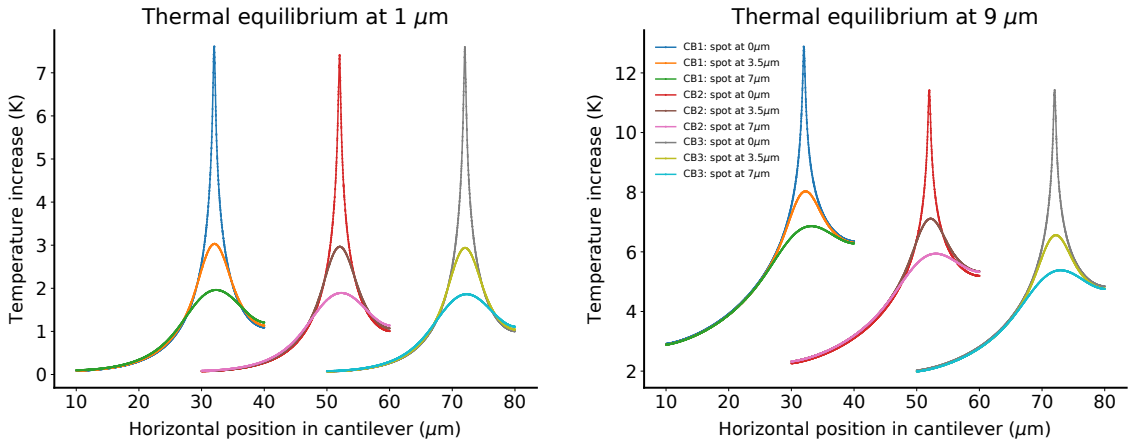

Figure 4.8: Linear x-direction qp-BioAc cantilever's temperature increase profile considering a confocal light source with a wavelength of 488 nm and a total power of 1 mW.

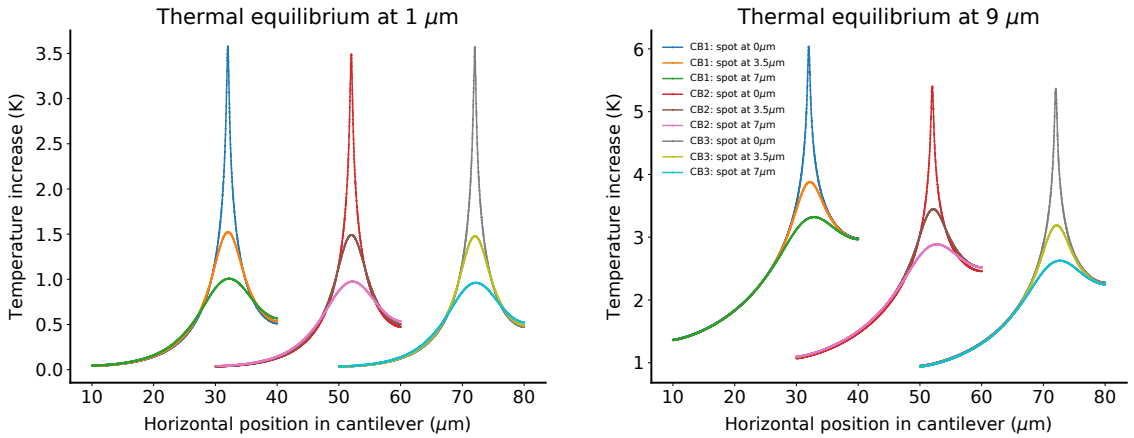

Figure 4.9: Linear x-direction qp-BioAc cantilever's temperature profile considering a confocal light source with a wavelength of 532 nm and a total power of 1 mW.

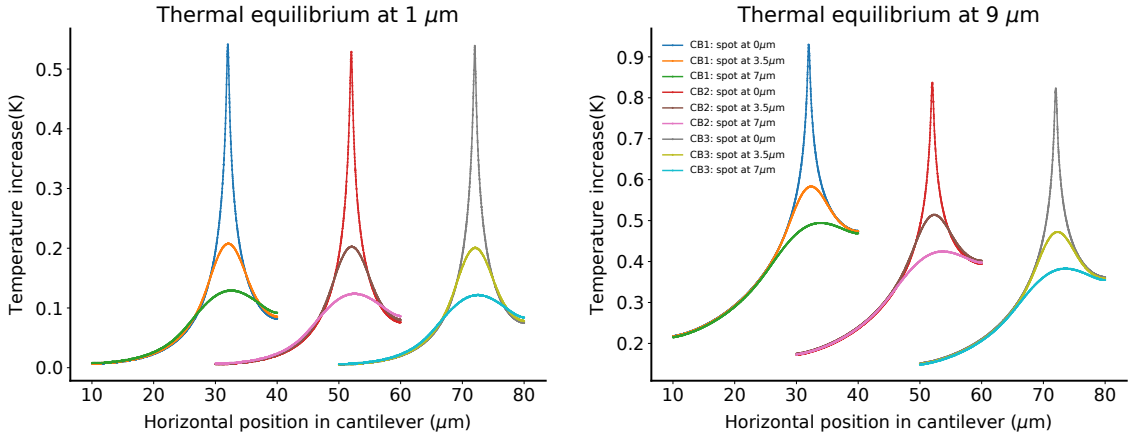

Figure 4.10: Linear x-direction qp-BioAc cantilever's temperature increase profile considering a confocal light source with a wavelength of 633 nm and a total power of 1 mW.

Due to the big amount of data, in case of qp-BioAc cantilevers, the maximum temperature increases reached in the different confocal illumination optical situations and considering the 2 different boundary conditions imposed are presented in table 4.1.

4.3 Maximum temperatures overview

In order to evaluate better the relationship between the maximum temperature increases reached and the different optical conditions, this section gathers all the maximum temperature increases provided by the whole previously presented results.

Table 4.1: Maximum temperature increases reached in qp-BioAc cantilevers considering different confocal illumination optical simulations. The results consider the two stated equilibrium situations: equilibrium at 1 (Tinc1) and 9 (Tinc9) μm below the cantilevers.

Cantilever	Wavelength (nm)	Spot distance (μm)	Tinc1 (K)	Tinc9 (K)
CB1	405	0	8.72	14.27
		3.5	3.71	9.09
		7	2.25	7.82
	488	0	7.61	12.89
		3.5	3.03	8.03
		7	1.96	6.86
	532	0	3.58	6.04
		3.5	1.52	3.88
		7	1.01	3.32
	633	0	0.51	0.93
		3.5	0.21	0.58
		7	0.13	0.49
CB2	405	0	8.49	12.64
		3.5	3.64	8.10
		7	2.42	6.83
	488	0	7.41	11.42
		3.5	2.97	7.11
		7	1.89	5.94
	532	0	3.49	5.40
		3.5	0.49	3.45
		7	0.97	2.89
	633	0	0.53	0.84
		3.5	0.20	0.51
		7	0.12	0.43
CB3	405	0	8.78	12.89
		3.5	3.61	7.52
		7	2.39	6.23
	488	0	7.60	11.43
		3.5	2.94	6.56
		7	1.86	5.38
	532	0	3.57	5.37
		3.5	1.48	3.19
		7	0.96	2.63
	633	0	0.54	0.82
		3.5	0.20	0.47
		7	0.12	0.38

For widefield illumination the maximum temperature increases are presented on table 4.2.
In case of confocal illumination due to the high number of different combinations of set-ups, the maximum temperature reached versus the confocal spot distance for the 4 different cantilevers are plotted, considering the 4 different wavelengths and the two established distances for thermal equilibrium: 1 and 9 μm.
The table 4.2 presents the maximum temperature increases reached in widefield illumination schemes considering the 4 different cantilever models and the 2 different boundary conditions applied.
The figures 4.11 and 4.12 present the plots of the maximum temperature increases reached in confocal illumination simulations versus the confocal spot distance from the gold coating considering a thermal equilibrium at 1 and 9 μm below the cantilever respectively.

Table 4.2: Maximum temperature increase reached in the simulated widefield set-ups. It is considered a thermal equilibrium at 1 (Tinc1) and 9 (Tinc9) μm below the cantilever.

Cantilever	Tinc1 (K)	Tinc9 (K)
PNP-TR	0.06	0.44
CB1	0.05	0.32
CB2	0.05	0.32
CB3	0.05	0.33

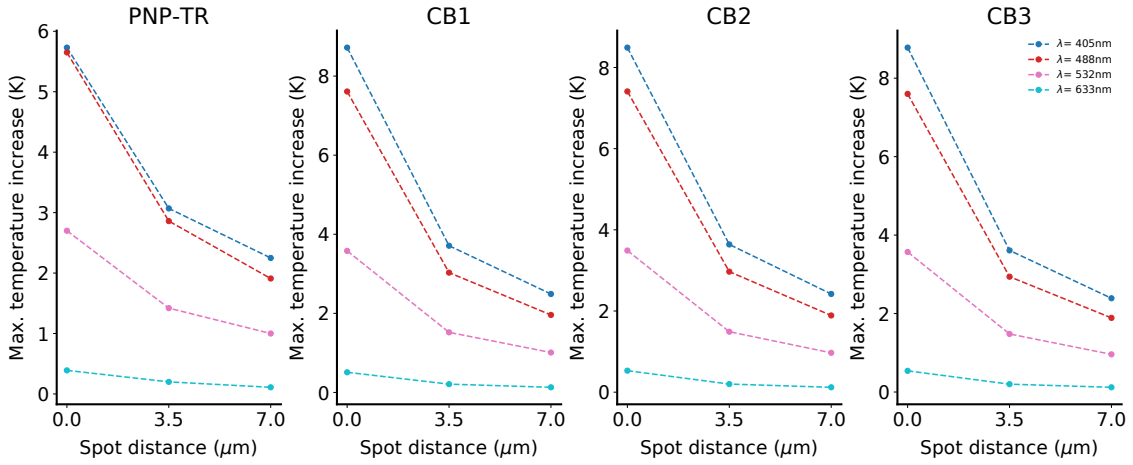

Figure 4.11: Maximum temperature increase reached in confocal illumination set-ups versus the confocal spot distance from the gold coating for the different cantilevers and wavelengths. It is considered a thermal equilibrium at 1 μm below the cantilever.

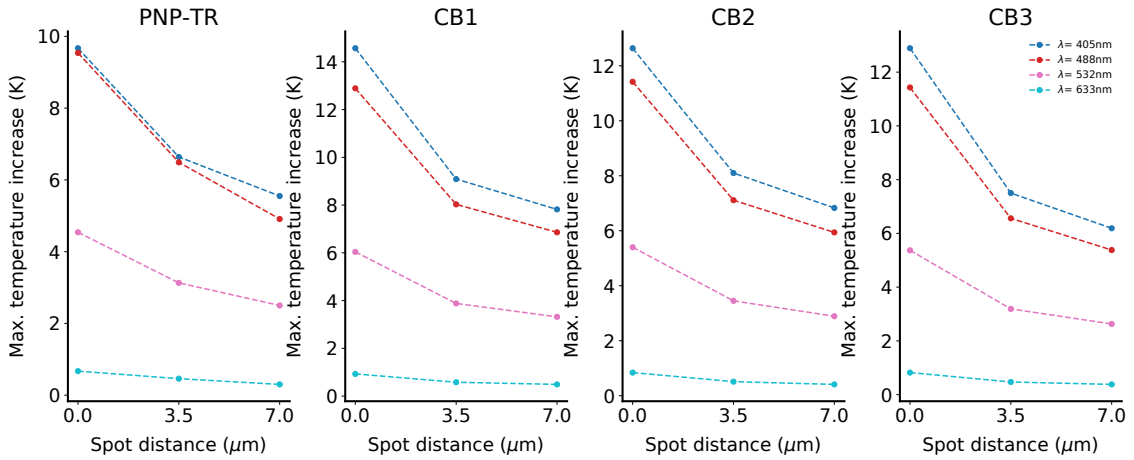

Figure 4.12: Maximum temperature increase reached in confocal illumination set-ups versus the confocal spot distance from the gold coating for the different cantilevers and wavelengths. It is considered a thermal equilibrium at 9 μm below the cantilever.

4.4 Discussion

The presented results provide resultant temperature profiles of illuminating four different cantilevers with the illumination set-up introduced by Miranda et al. [1] and with a 1 mw confocal lights with 405, 488, 532 and 633 nm of wavelength focusing on 3 different vertical positions.

Assumptions regarding the surrounding water's temperature cannot be made (even if one considers to put a monitor measuring the water's temperature) due to the fact that these simulations aim to model the heat propagation in solids which fails taking in account phenomena such as boiling and fluid's movement [39]. Nonetheless, the model is physically acceptable in the boundaries between the cantilever and the surrounding water since the selected values for the density, specific heat and thermal conductivity relate to liquid water, ensuring that the heat changes in those interfaces are well modeled. Furthermore, the convection boundary condition applied on the interfaces between solids and the water contributes to a better model.

In case of widefield illumination of a PNP-TR cantilever it was obtained a temperature difference from the environment of 0.06 K considering the thermal equilibrium to happen 1 μm away from the cantilever's down surface and a temperature difference of 0.44 K considering the thermal equilibrium to happen 9 μm away from the cantilever's down surface. the last result is more consistent with the 0.33 K difference pointed by Miranda et al. [1], although their preview carries some error due to the model used by them (*cf.* appendix A). In case of the

qp-BioAc we have a temperature difference of 0.09 K and 0.32 K, considering respectively a thermal equilibrium at 1 and 9 μm away from the cantilever's lower surface, respectively.
In a confocal illumination scheme we have the maximum temperature differences from the environment for the 405 nm wavelength illumination which can be about 5.7 and 8.9 K for PNP-TR and qp-BioAc cantilevers respectively, considering a thermal equilibrium at 1 μm. For a thermal equilibrium at 9 μm we have differences of 9.5 and 12.85 K for PNP-TR and qp-BioAc cantilevers respectively.
For a 488 nm confocal illumination we have a bit lower temperature differences, which differ by a maximum of 1 K, from the previous.
The maximum temperatures generated by a 532 nm confocal illumination are much lower than the temperatures generated by the 405 and 488 nm illuminations, having a maximum difference from these of about 4 K.
The 633 nm confocal illumination leads to maximum temperature increase, in Kelvin, lower than a unity.
Finally it is clear by the figures 4.11 and 4.12 that the maximum temperature reached in all the cases is highly dependent on the vertical position of the confocal spot.

Chapter 5

Conclusions and further work

In this work it was studied, through computational simulations, the impact of illuminating AFM cantilevers with different illumination schemes in combined AFM/optical microscopy set-ups when it comes to their operation temperature. These combined setups have been highly developed and investigated in the live cell imaging field in order to extend the applications and capabilities of both solo AFM and optical microscopy techniques and have been pointed out as future potential tools to unveil new processes and dynamics in biological systems.
Many biological processes and molecular dynamics are highly dependent on the environment temperature, reason why, the experiments in this field are performed at a controlled temperature (310.15 K when it comes to mammalian cells).
The combination of AFM with optical microscopy techniques can lead to a temperature increase in the AFM cantilever due to the light interaction of the light with the gold coating of the cantilever, usually required to enhance the reflectivity in liquid media. The need of understanding the possible temperatures that these systems can achieve arises.
A set of optical and thermal simulations (using Lumerical software) was performed in order to understand the temperatures that can be reached by illuminating PNP-TR and qp-BioAc cantilevers with both widefield an confocal light.
It is concluded that in some cases the confocal illumination (1mw) can lead to temperature increases higher than 5 K, which can be very significant.
In the simulated widefield set-up developed by Miranda et al. [1] the temperature increase evaluated was less than 1 K and concordant with the value pointed by them in their publication, which makes this set-up a promising tool when keeping

the environment temperature is crucial.
It is clear by the provided results that the confocal spot interacts strongly with the cantilever's gold coating in all the cases, which implies that care has to be taken when combining AFM with confocal illumination optical set-ups to acquire information highly dependent on the temperature.
Furthermore, it can be pointed by the optical simulations that the the gold coating absorbs a big amount of the incident light in the 350-550 nm region, which can lead to fluorescence quenching effects.
This work may be continued with further experimental studies which would be pertinent in one way to validate the simulations developed and in other way to calibrate the boundary conditions in order to have a correspondence between the simulated and experimental systems. Once calibrated these simulations can be expanded to address similar questions in other experimental set-ups with different cantilevers and light sources.
Although there are some very promising nanoscale temperature mapping approaches [40–42], the scanning thermal microscopy (SthM) was already used to measure temperature increase in plasmonic nanostructures [4], which can be considered similar to AFM cantilevers, making this technique a potential candidate to be used in future studies.
Furthermore, there are experiments ongoing by using polarization anisotropy, based on the work presented by Donner et al. [43].

Bibliography

1. Miranda, A., Martins, M. & De Beule, P. A. Simultaneous differential spinning disk fluorescence optical sectioning microscopy and nanomechanical mapping atomic force microscopy. *Review of Scientific Instruments* **86.** ISSN: 10897623. http://dx.doi.org/10.1063/1.4931064 (2015).

2. Gómez-Varela, A. I., Stamov, D. R., Miranda, A., Alves, R., Barata-Antunes, C., Dambournet, D., Drubin, D. G., Paiva, S. & De Beule, P. A. A. Simultaneous co-localized super-resolution fluorescence microscopy and atomic force microscopy: combined SIM and AFM platform for the life sciences. *Scientific Reports* **10,** 1122. ISSN: 2045-2322. http://www.nature.com/articles/s41598-020-57885-z (2020).

3. Fernandes, T. F. D., Saavedra, O., Margeat, E., Milhiet, P.-E. & Costa, L. Synchronous, Crosstalk-free Correlative AFM and Confocal Microscopies/Spectroscopies. *Scientific Reports*, 1–12. ISSN: 20452322 (2020).

4. Desiatov, B., Goykhman, I. & Levy, U. Direct temperature mapping of nanoscale plasmonic devices. *Nano Lett.* **14,** 648–652. ISSN: 15306984 (2014).

5. Binnig, G., Quate, C. F. & Gerber, C. Atomic Force Microscope. *Physical Review Letters* **56,** 930–933. ISSN: 0031-9007. https://link.aps.org/doi/10.1103/PhysRevLett.56.930 (1986).

6. Binnig, G., Gerber, C., Stoll, E., Albrecht, T. R. & Quate, C. F. Atomic resolution with atomic force microscope. *Epl* **3,** 1281–1286. ISSN: 12864854 (1987).

7. McClelland, G. M., Erlandsson, R. & Chiang, S. in *Review of Progress in Quantitative Nondestructive Evaluation* 1307–1314 (Springer US, Boston, MA, 1987). http://link.springer.com/10.1007/978-1-4613-1893-4%7B%5C_%7D148.

8. *Springer Handbook of Nanotechnology* (ed Bhushan, B.) ISBN: 978-3-642-02524-2. http://link.springer.com/10.1007/978-3-642-02525-9 (Springer Berlin Heidelberg, Berlin, Heidelberg, 2010).

9. Dufrêne, Y. F., Ando, T., Garcia, R., Alsteens, D., Martinez-Martin, D., Engel, A., Gerber, C. & Müller, D. J. Imaging modes of atomic force microscopy for application in molecular and cell biology. *Nature Nanotechnology* **12,** 295–307. ISSN: 17483395. http://dx.doi.org/10.1038/nnano.2017.45 (2017).

10. Moreno Flores, S. & Toca-Herrera, J. L. The new future of scanning probe microscopy: Combining atomic force microscopy with other surface-sensitive techniques, optical microscopy and fluorescence techniques. *Nanoscale* **1,** 40–49. ISSN: 20403364 (2009).

11. Kassies, R., Van Der Werf, K. O., Lenferink, A., Hunter, C. N., Olsen, J. D., Subramaniam, V. & Otto, C. Combined AFM and confocal fluorescence microscope for applications in bio-nanotechnology. *Journal of Microscopy* **217,** 109–116. ISSN: 00222720 (2005).

12. Mathur, A. B., Truskey, G. A. & Reichert, W. M. Atomic force and total internal reflection fluorescence microscopy for the study of force transmission in endothelial cells. *Biophysical Journal* **78,** 1725–1735. ISSN: 00063495. http://dx.doi.org/10.1016/S0006-3495(00)76724-5 (2000).

13. Hu, D., Micic, M., Klymyshyn, N., Suh, Y. D. & Lu, H. P. Correlated topographic and spectroscopic imaging beyond diffraction limit by atomic force microscopy metallic tip-enhanced near-field fluorescence lifetime microscopy. *Review of Scientific Instruments* **74,** 3347–3355. ISSN: 00346748 (2003).

14. Dubreuil, F., Elsner, N. & Fery, A. Elastic properties of polyelectrolyte capsules studied by atomic-force microscopy and RICM. *European Physical Journal E* **12,** 215–221. ISSN: 12928941 (2003).

15. Picart, C., Senger, B., Sengupta, K., Dubreuil, F. & Fery, A. Measuring mechanical properties of polyelectrolyte multilayer thin films: Novel methods based on AFM and optical techniques. *Colloids and Surfaces A: Physicochemical and Engineering Aspects* **303,** 30–36. ISSN: 09277757 (2007).

16. Yu, J. Q., Yuan, J. H., Zhang, X. J., Liu, J. L. & Fang, X. H. Nanoscale imaging with an integrated system combining stimulated emission depletion microscope and atomic force microscope. *Chinese Science Bulletin* **58,** 4045–4050. ISSN: 10016538 (2013).

17. Chacko, J. V., Canale, C., Harke, B. & Diaspro, A. Sub-Diffraction Nano Manipulation Using STED AFM. *PLoS ONE* **8.** ISSN: 19326203 (2013).

18. Monserrate, A., Casado, S. & Flors, C. Correlative atomic force microscopy and localization-based super-resolution microscopy: Revealing labelling and image reconstruction artefacts. *ChemPhysChem* **15,** 647–650. ISSN: 14397641 (2014).

19. Zhou, L., Cai, M., Tong, T. & Wang, H. Progress in the Correlative Atomic Force Microscopy and Optical Microscopy. *Sensors* **17,** 938. ISSN: 1424-8220. http://www.mdpi.com/1424-8220/17/4/938 (2017).

20. Odermatt, P. D., Shivanandan, A., Deschout, H., Jankele, R., Nievergelt, A. P., Feletti, L., Davidson, M. W., Radenovic, A. & Fantner, G. E. High-Resolution Correlative Microscopy: Bridging the Gap between Single Molecule Localization Microscopy and Atomic Force Microscopy (2015).

21. Allen, J. R. & Ross, S. T. STORM without enzymatic oxygen scavenging for correlative atomic force and fluorescence superresolution microscopy STORM without enzymatic oxygen scavenging for correlative atomic force and fl uorescence superresolution microscopy (2018).

22. Timoshenko, S. Analysis of Bi-Metal Thermostats. *Journal of the Optical Society of America* **11,** 233. ISSN: 0030-3941. https://www.osapublishing.org/abstract.cfm?URI=josa-11-3-233 (1925).

23. *High-Performance Photonic Simulation Software - Lumerical* https://www.lumerical.com/ (2020).

24. Griffiths, D. J. *Introduction to Electrodynamics* ISBN: 9781108420419. https://www.cambridge.org/core/product/identifier/9781108333511/type/book (Cambridge University Press, 2017).

25. *FDTD product reference manual – Lumerical Support* https://support.lumerical.com/hc/en-us/articles/360033154434-FDTD-product-reference-manual (2020).

26. *HEAT product reference manual – Lumerical Support* https://support.lumerical.com/hc/en-us/articles/360037224694 (2020).

27. Kane Yee. Numerical solution of initial boundary value problems involving maxwell's equations in isotropic media. *IEEE Transactions on Antennas and Propagation* **14,** 302–307. ISSN: 0018-926X. http://link.springer.com/10.1007/978-3-319-61185-3%7B%5C_%7D17%20http://ieeexplore.ieee.org/document/1138693/ (1966).

28. Lesina, A. C., Vaccari, A., Berini, P. & Ramunno, L. On the convergence and accuracy of the FDTD method for nanoplasmonics. *Opt. Express* **23,** 10481. ISSN: 1094-4087 (2015).

29. Jackson, J. D. *Classical Electrodynamics* 3rd ed. ISBN: 978-0-471-30932-1 (John Wiley & Sons, 1999).

30. *Understanding frequency domain CW normalization – Lumerical Support* https://support.lumerical.com/hc/en-us/articles/360034394234 (2020).

31. *Understanding the non-uniform mesh in FDTD – Lumerical Support* https://support.lumerical.com/hc/en-us/articles/360034382634-Understanding-the-non-uniform-mesh-in-FDTD (2020).

32. *PNP-TR - NanoWorld* https://www.nanoworld.com/pyrex-nitride-triangular-silicon-nitride-cantilever-afm-tip-pnp-tr%7B%5C#%7Dvideo1 (2020).

33. *qp-BioAc - Nanosensors* https://www.nanosensors.com/uniqprobe-uniform-quality-contact-or-dynamic-mode-for-biology-in-dynamic-ac-mode-afm-tip-qp-BioAC (2020).

34. *Convergence testing process for FDTD simulations* https://support.lumerical.com/hc/en-us/articles/360034915833-Convergence-testing-process-for-FDTD-simulations (2020).

35. *Understanding field truncation issues with finite sized plane wave sources – Lumerical Support* https://support.lumerical.com/hc/en-us/articles/360034382874-Understanding-field-truncation-issues-with-finite-sized-plane-wave-sources (2020).

36. Wolf, E. Electromagnetic diffraction in optical systems. I. An integral representation of the image field. *Proceedings of the Royal Society of London. Series A. Mathematical and Physical Sciences* **253,** 349–357 (1959).

37. Richards, B. & Wolf, E. Electromagnetic diffraction in optical systems. II. Structure of the image field in an aplanatic system. *Proceedings of the Royal Society of London. Series A. Mathematical and Physical Sciences* **253,** 358–379 (1959).

38. *Symmetric and anti-symmetric BCs in FDTD and MODE – Lumerical Support* https://support.lumerical.com/hc/en-us/articles/360034382694-Symmetric-and-anti-symmetric-BCs-in-FDTD-and-MODE (2020).

39. *Photocatalysis – Lumerical Support* https://support.lumerical.com/hc/en-us/articles/360042274854-Photocatalysis (2020).

40. Mecklenburg, M., Hubbard, W. A., White, E. R., Dhall, R., Cronin, S. B., Aloni, S. & Regan, B. C. Nanoscale temperature mapping in operating microelectronic devices. *Science (80-.).* **347,** 629–632. ISSN: 10959203 (2015).

41. Menges, F., Mensch, P., Schmid, H., Riel, H., Stemmer, A. & Gotsmann, B. Temperature mapping of operating nanoscale devices by scanning probe thermometry. *Nat. Commun.* **7.** ISSN: 20411723 (2016).

42. Baffou, G., Kreuzer, M. P., Kulzer, F. & Quidant, R. Temperature mapping near plasmonic nanostructures using fluorescence polarization anisotropy. *Opt. Express* **17,** 3291. ISSN: 1094-4087. https://www.osapublishing.org/oe/abstract.cfm?uri=oe-17-5-3291 (Mar. 2009).

43. Donner, J. S., Thompson, S. A., Kreuzer, M. P., Baffou, G. & Quidant, R. Mapping Intracellular Temperature Using Green Fluorescent Protein. *Nano Letters* **12,** 2107–2111 (2012).

Appendix A

Timoshenko model for bimorph cantilevers

The following model was originally presented by Timoshenko [22] with the purpose of describing the bending of a bi-metal strip (used as a thermostat) submitted to a uniform heating. This analysis gives us a mathematical model that calculates the deflection of a bimorph cantilever (a cantilevered device consisting of two layers) when uniformly heated from a temperature T_0 to T. It has been made on the assumption that cross-section of the cantilever remains plane and perpendicular to the curved axis during the heating process. It is also assumed that the width of the strip is very small and it is only considered the elongation in longitudinal direction (the elongation in transverse directions can be neglected due to the geometry), which allows the analysis to be made using the linear thermal expansion coefficients. Because of the different linear thermal expansion coefficients of the two layers, when a bimorph cantilever is heated it bends due to the different rate at which each layer expands (Fig.A.1). In case of AFM cantilevers designed to operate in liquid media, the bending is always downwards because of the fact that metals have higher thermal expansion coefficients than silicon or silicon nitride [3].

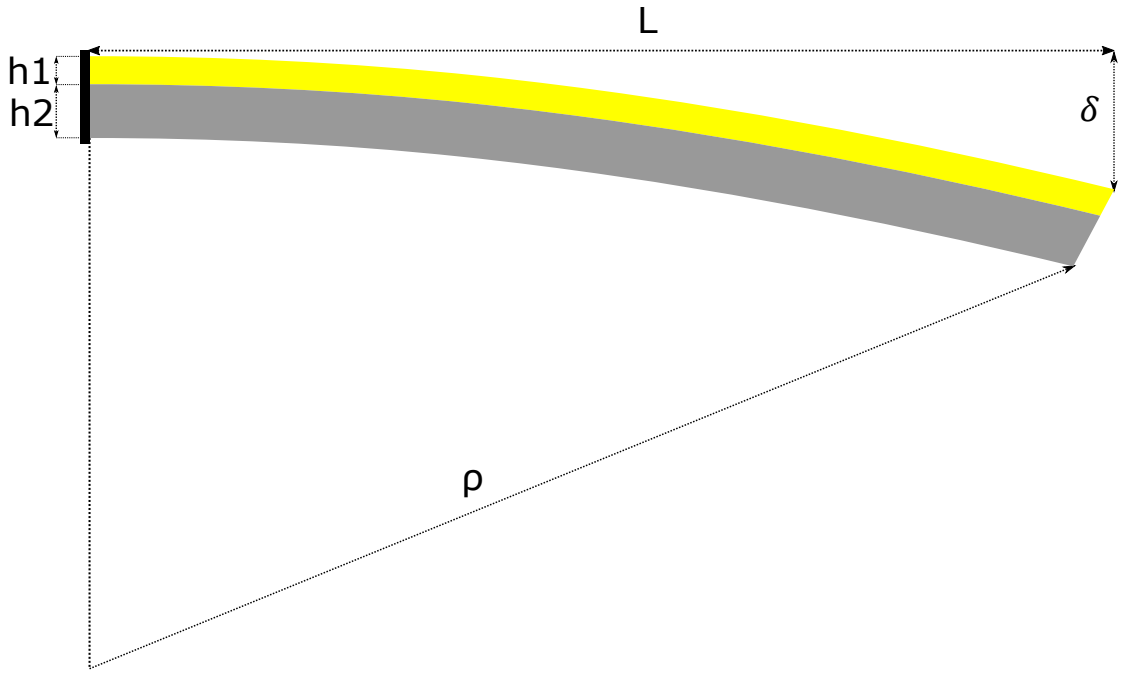

Figure A.1: Bending of a bi-metallic strip geometrical representation. L stands for cantilever's length, h1 and h2 for the thickness of layer 1 (yellow) and layer 2 (gray) respectively, δ for deflection and ρ for radius of curvature.

From Timoshenko [22] we have:

$$\frac{1}{\rho} = \frac{(\alpha_2 - \alpha_1)(T - T_0)}{\frac{(h_1+h_2)}{2} + \frac{2(E_1 I_1 + E_2 I_2)}{(h_1+h_2)}\left(\frac{1}{E_1\alpha_1} + \frac{1}{E_2\alpha_2}\right)}, \tag{A.1}$$

where α_1 and α_2 are the linear thermal expansion coefficients of each layer and the E_1 and E_2 are their Young's module. I_1 and I_2 are the area moment of inertia of each layer therefore in this case we have (in this model the width of the cantilever is taken as equal to unity):

$$I_1 = \frac{h_1^2}{12}, \quad I_2 = \frac{h_2^2}{12}. \tag{A.2}$$

From a geometric point of view we should notice that we can form a right triangle with sides L, ρ and $(\rho - \delta)$.Therefore, by Pythagorean theorem, we can conclude that:

$$\begin{aligned} \rho^2 &= L^2 + (\rho - \delta)^2 \\ \Leftrightarrow L^2 &= \delta(2\rho - \delta) \end{aligned} \tag{A.3}$$

We can write the deflection (δ) as a function of radius of curvature (ρ) and length (L), by considering that deflection is very small compared to the radius of curvature, which leads to:

$$\delta = \frac{L^2}{2\rho} \tag{A.4}$$

Finally, considering equations A.1 and A.4 we can write the equation that gives the deflection as function of Temperature change ($\Delta T = T - T_0$):

$$\delta = 3(\alpha_1 - \alpha_2)\frac{h_1 + h_2}{h_2^2}\left[4 + 6\left(\frac{h_1}{h_2}\right) + 4\left(\frac{h_1}{h_2}\right)^2 + \frac{E_1}{E_2}\left(\frac{h_1}{h_2}\right)^3 + \frac{E_2}{E_1}\left(\frac{h_2}{h_1}\right)\right]^{-1} L^2 \Delta T, \tag{A.5}$$

Which is the equation used by Miranda et al. [1] to calculate a temperature change with a measured value of deflection.